# Impacts of atmospheric circulation patterns and cloud inhibition on aerosol radiative effect and boundary layer structure during winter air pollution in Sichuan Basin, China

Hua Lu[1,3],Min Xie[2],Tijian Wang[1], Bojun Liu[4], Yangzhihao Zhan[1], Bingliang Zhuang[1], Shu Li[1], Mengmeng Li[1], Kuanguang Zhu[1,5]

[1]School of Atmospheric Sciences, Nanjing University, Nanjing 210023, China
[2]School of Environment, Nanjing Normal University, Nanjing 210023, China
[3] Chongqing Institute of Meteorological Sciences, Chongqing 401147, China
[4]Chongqing Meteorological Observatory, Chongqing 401147, China
[5]Hubei Provincial Academy of Eco-environmental Sciences, Wuhan 430079, China

# Impacts of atmospheric circulation patterns and cloud inhibition on aerosol radiative effect and boundary layer structure during winter air pollution in Sichuan Basin, China

Hua Lu[1,3], Min Xie[2], Tijian Wang[1], Bojun Liu[4], Yangzhihao Zhan[1], Bingliang Zhuang[1], Shu Li[1], Mengmeng Li[1], Kuanguang Zhu[1,5]

[1]School of Atmospheric Sciences, Nanjing University, Nanjing 210023, China

[2]School of Environment, Nanjing Normal University, Nanjing 210023, China

[3]Chongqing Institute of Meteorological Sciences, Chongqing 401147, China

[4]Chongqing Meteorological Observatory, Chongqing 401147, China

[5]Hubei Provincial Academy of Eco-environmental Sciences, Wuhan 430079, China

*Correspondence to*: Min Xie (minxie@njnu.edu.cn)

**Abstract.** Winter persistent aerosol pollution frequently occurs in the Sichuan Basin (SCB) due to its unfavorable weather conditions, such as low wind, wetness, and cloudiness. Based on long–term observational data analyses from 2015–2021, it has been found that the four representative stations in the SCB often simultaneously experience $PM_{2.5}$ pollution accompanied by variations in meteorological conditions above 850 hPa, which indicates a connection between regional winter air pollution in the SCB and large–scale synoptic patterns. The dominant 850 hPa synoptic patterns of winter SCB were classified into six patterns using T–model principal component analysis: (1) strong high pressure in the north, (2) east high west low (EHWL) pressure, (3) weak high pressure in the north, (4) weak ridge of high pressure after the trough, (5) low trough (LT), and (6) strong high pressure. Pattern 2 characterized with EHWL pressure system, and Pattern 5 featured with LT, were identified as key synoptic patterns for the beginning and accumulation of pollution processes. Pattern 1, characterized by a strong high pressure in the north, was the cleanest pattern associated with reduced $PM_{2.5}$ concentrations. The EHWL and LT patterns were associated with a remarkably high cloud liquid content, attributed to upper southerly winds introducing humid air. Clouds reduce solar radiation through reflection and scattering, resulting in more stable stratification and aerosol accumulation. This cloud radiation interaction (CRI) was more pronounced in the LT pattern due to denser isobaric lines and stronger southerly winds than in the EHWL pattern. Numerical simulation experiments utilizing WRF-Chem indicated that there is a upper-level heating during afternoon and surface cooling in the morning forced by the aerosol radiation interaction (ARI) under the EHWL and LT patterns. Additionally, strong surface cooling in the evening influenced by valley winds could be found. With wet and cloudy synoptic forcing, ARI directly affects the stability of the boundary layer and is modulated through CRI inhibition. For example, Chongqing exhibited lower $PM_{2.5}$ concentrations and stronger ARI compared to the western and southern SCB due to lower cloud liquid content and weaker CRI inhibition on ARI. The CRI inhibition caused a 50 % reduction in solar radiation and boundary layer height during the daytime under the LT pattern, which was larger than that under the EHWL

39    pattern. This study comprehensively analyzed the spatial disparities in cloud inhibition on ARIs, their
40    impacts on the boundary layer structure, and the discrepancies of these interactions under different
41    synoptic patterns during pollution processes. The findings hold important implications for effective
42    management of pollution processes in cloudy and foggy weather.

43    Key words: Synoptic patterns, Cloud radiation interaction inhibition, Aerosol radiation interaction,
44    Boundary layer structure, Sichuan Basin.

45    **1 Introduction**

46      Particulate matter (PM) pollution has become a significant environmental concern in China (Xie
47    et al., 2016a; 2016b; Che et al., 2019). High concentrations of aerosols not only worsen air quality
48    and pose serious health risks to residents, but also have implications for weather and climate
49    through their effects on radiation and clouds (Li et al., 2019; Zhao et al., 2020; Alexeeff et al.,
50    2021; Yang et al., 2021). The interactions between aerosols and clouds present the largest
51    uncertainty in anthropogenic radiative forcing of the Earth's climate (Liao et al., 2017; Haywood
52    et al., 2021). Studying interactions among cloud, aerosol and radiation from an air quality perspective
53    is crucial for a scientific understanding of relationship between weather and pollution.
54      Excessive emissions are the essential cause of air pollution, with primary aerosol and secondary
55    aerosol formation playing significant roles in comprehending the complete picture of air pollution
56    (Peng et al., 2021). Besides, meteorological conditions not only influence on the formation of
57    secondary aerosols, but also govern the transportation and distribution of both primary and
58    secondary aerosols, and thereby impact regional and long-range air pollution (Zhu et al., 2018;
59    Luo et al., 2018; Nichol et al., 2020; Zhang et al., 2020; Jiang et al., 2021). PM and gaseous
60    pollutants, primarily transported by the planetary boundary layer (PBL), are directly or indirectly
61    influenced by various meteorological factors such as wind, relative humidity, PBL height (PBLH),
62    and solar radiation. These factors contribute to the multi–temporal and spatial distribution
63    characteristics through vertical and horizontal diffusion, physicochemical reactions, and dry and
64    wet deposition (Park et al., 2017; Shu et al., 2017; Zhan et al., 2019; Huang et al., 2019). Large–
65    scale synoptic forcing is considered the primary driving condition for meteorological factors, PBL
66    structure, and the resulting distribution of atmospheric pollutants (Miao et al., 2019; Ning et al.,
67    2019; Jiang et al., 2020; Li et al., 2021). Specific synoptic patterns can induce advection, which
68    largely determines the local PBL structure and development. PBL, located at the bottom of the
69    atmosphere, is responsible for the main exchange of heat, moisture, and matter between the surface
70    and the free troposphere (Stull, 1988). The fate of pollutants emitted near the surface, a significant
71    source of aerosols in the air, is largely controlled by the PBL (Garratt, 1994). The PBLH is often
72    used as a metric to characterize the capacity and dilution of pollutants (Seidel et al., 2010).
73    Synoptic patterns can directly determine the meteorological conditions of emitted pollutants and
74    influence their transport by regulating PBL thermal stratification and mechanical turbulence (Stull,
75    1988; Ning et al., 2018; Zhan et al., 2019; Jiang et al., 2021; Zhang et al., 2022).

Unfavorable meteorological conditions play a significant role in contributing to aerosol pollution. When pollutants accumulate to a certain degree, aerosols can reduce surface solar radiation through backscattering or absorbing solar radiation, leading to surface cooling. This decrease in solar radiation and temperature near the ground weakens turbulent diffusion, suppresses the convective development of the PBL, and lowers PBLH, which in turn exacerbates aerosol pollution (Ding et al., 2016; Wang et al., 2018). Moreover, the increase in humidity caused by the decreased surface saturation vapor pressure and inhibited water vapor diffusion enhances aerosol hygroscopic growth accelerates liquid–phase and heterogeneous reactions, and contributes to aerosol pollution (Pilinis et al., 1989). The positive feedback between unfavorable PBL meteorology and increasing aerosols was found to be responsible for the majority of the increase in $PM_{2.5}$ during cumulative stages in various regions of eastern China affected by aerosol pollution, including the North China Plain, the Guanzhong Plain, the Yangtze River Delta, the Two Lakes Basin, the Pearl River Delta and the Northeast China Plain. But in the Sichuan Bain (SCB), the feedback is weak due to the suppression of the cloudy mid-upper layer (Zhong et al., 2018; Zhong et al., 2019). As for the aerosol-cloud interactions, arise from increasing aerosols acting as cloud condensation nuclei in cloud and translating into larger concentrations of smaller cloud droplets, leading to an increased cloud albedo reflecting more radiation back to space (Twomey, 1977; Lohmann and Feichter, 2005). Even a marginal increase in cloud droplets above pristine conditions in deep convective clouds causes more droplets to reach supercooled levels, which enhances latent heat release and invigorates convection (Rosenfeld et al., 2009; Possner et al., 2015). Further increases in cloud droplets result in direct radiative effects, reducing downward solar radiation, cooling the surface, and inhibiting convection (Scott et al., 2016).

The SCB is surrounded by high mountains with cloudy and wet weather conditions. The mean annual relative humidity in the SCB is around 75%, with cloud fraction exceeding 80%, and an average of 1200 hours of sunshine per year. The Chengdu–Chongqing city cluster in the SCB serves as the economic center of the upper reaches of the Yangtze River in China, accounting for approximately 10 % of the country's population. However, rapid industrialization and urbanization in this region have resulted in severe air pollution. The SCB is recognized as one of the most polluted regions in China, with high black carbon concentrations (Li et al., 2016; Cao et al., 2021). The Qinghai–Tibet Plateau on the western edge of the SCB significantly influences the transport and accumulation of pollutants through thermal and dynamic effects (Ning et al., 2017; Shu et al., 2021). In addition, the Qinghai–Tibet topography leads to higher cloud water content over the SCB than the other regions (Yu et al., 2004; Yang et al., 2012). Many studies have emphasized the importance of the interactions between cloud, aerosols and radiation in air pollution processes (Wang et al., 2018; Hu et al., 2021). High pollutant emissions, combined with the prevalence of cloudy and foggy weather, make these interactions in the SCB even more complex than those in other regions. The aerosol radiation interactions (ARI) can be inhibited by cloud in cities like Chengdu (Zhong et al., 2019). However, there is a lack of in-depth quantitative discussions regarding this aspects in the SCB. On one hand, the complex terrain in the SCB leads to differences in the meteorological conditions

115 between them (Ning et al., 2017; Lu et al., 2022). For example, Chengdu is a typical basin city while
116 Chongqing is a mountain city located on the basin slope, so they have markedly different climate
117 conditions. It remains to be elucidated whether these conditions will result in spatial disparities in cloud
118 inhibition on the ARI. On the other hand, synoptic forcing, as the primary driver of meteorological
119 variations, undoubtedly play an unneglectable role in shaping cloud cover and boundary layer
120 structures (Miao et al., 2020; Wang et al., 2022; Painemal et al., 2023). The discrepancies in cloud
121 inhibition on ARI under different synoptic patterns also need to be revealed. Addressing these issues is
122 crucial for understanding the persistent pollution processes and the intricate interactions between
123 weather and pollution in the SCB. It holds important implications for the effective management of
124 pollution processes in cloudy and foggy weather.

125     Characterized with high aerosol loadings and semi–permanent cloudy weather, the SCB
126 provides an ideal region for studying the complex interactions between clouds, aerosols, and the
127 PBL. This study objectively classifies the synoptic patterns influencing the SCB based on long–
128 term  data. By conducting an integrated analysis of pollutants and meteorological factors, the
129 primary pollution sources and clean synoptic patterns are identified. To further investigate the
130 inhibition of cloud radiation interaction (CRI) on ARI under different synoptic patterns in the SCB,
131 WRF–CHEM simulation experiments are conducted. The results contribute to a deeper
132 understanding of CRI, ARI, and the PBL interactions in regions influenced by plateau–basin
133 topography with wet and cloudy weather. The data and methods are presented in Section 2,
134 whereas Section 3 describes the synoptic patterns and their corresponding impacts on clouds,
135 aerosols, radiation, and PBL. Finally, the conclusions are presented in Section 5.

136 **2 Data and method**

137 **2.1 Observation data**

138     Air quality monitoring data used in this study were obtained from air quality monitoring sites
139 established by the Ministry of Ecology and Environment of China across the SCB. Hourly $PM_{2.5}$
140 observations from 18 stations in the SCB were collected during the winter period from 2015 to 2021
141 for data analysis and model verification purposes (Fig. 1b). The abbreviations CQ, CD, MY, DY,
142 LS, MS, YA, ZY, ZG, YB, LZ, NJ, GA, NC, SN, GY, DZ, and BZ represent the following cities:
143 Chongqing, Chengdu, Mianyang, Deyang, Leshan, Meishan, Yaan, Ziyang, Zigong, Yibin,
144 Luzhou, Neijiang, Guangan, Nanchong, Suining, Guangyuan, Dazhou, and Bazhong, respectively.
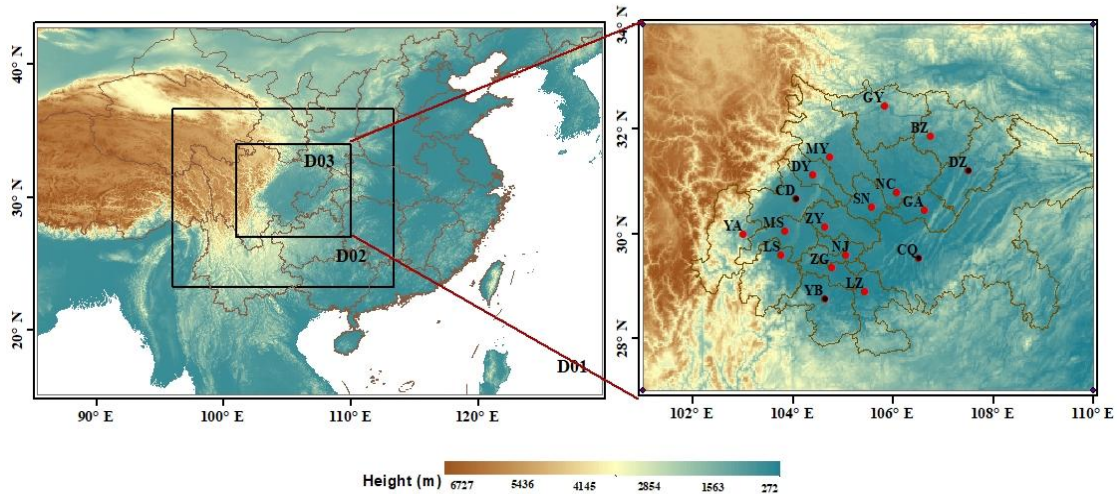
**Figure 1.** (a) Three layers of simulation domains in WRF-Chem with topography map as shading; (b) the locations of 18 air quality monitoring stations (red dots) and 4 sounding stations (black dots) in the Domain 3.

The SCB has four sounding stations: Wenjiang (CD), YB, DZ, and Shapingba (CQ), situated in the western, southern, northwestern, and eastern regions of the basin, respectively (Fig. 1b), and represent different pollution and meteorological conditions in different regions within the SCB. In all, the air pollution over the SCB exhibits a gradual decrease from southwest to northeast. Statistical analysis indicates that the western and the southern basin experience the most severe pollution. The western basin shows the highest pollution proportion, while the southern basin exhibits the highest occurrence of heavy pollution. In the northeastern basin, specifically in DZ, heavy pollution is more likely to occur during winter, which verifies it to be the third highest pollution zone outside the western and southern basin. This makes the spatial distribution during winter differs from the overall annual pollution pattern in the SCB (Lu et al., 2022; Qi et al., 2022). Regarding meteorological conditions, research reveals that DZ has the lowest ventilation coefficient during winter, while CQ has the highest. The SCB experiences frequent temperature inversions, with CD having a higher occurrence of inversions compared to the other three cities. CD also exhibits the strongest inversion intensity and is prone to multi-layer inversions. On the other hand, YB and CQ have greater inversion thickness, while CD has the smallest inversion thickness (Feng et al., 2020). The vertical distribution of the meteorological factors used in the study was obtained from an L–band sounding radar, collecting temperature, pressure, humidity, and wind data at 00:00 and 12:00 Coordinated Universal Time (UTC) on vertical levels every second from the surface up to 30 km. Ground observation data from the four cities, including temperature and dew point temperature, were used for meteorological factor simulation verification. All meteorological data were obtained from the China Weather Website Platform maintained by the China Meteorological Bureau. As for the calculation of PBLH, there are various methods to determine the PBLH, and differences in methods, data or threshold values may yield quite different PBLH results (Seibert et al., 2000; Eresmaa et al., 2006; Jiang et al., 2021). The bulk

170     Richardson number (*Ri*) method was adopted to calculate the PBLH with sounding data in

171     the study by assuming that the PBLH is the height at which *Ri* reaches its critical value (*Rc*).

172     *Ri* at a certain height *h* is calculated as follows:

173 $$Ri = \frac{(g/\theta_{v0})(\theta_{vh} - \theta_{v0})h}{u_h^2 + v_h^2}$$

174     Where g is the acceleration of gravity, $\theta_{v0}$ and $\theta_{vh}$ are the virtual potential temperature at surface

175     and the height *h*, respectively, and $u_h$ and $v_h$ are the meridional and zonal wind components at *h*.

176     We adopted the *Ri* method and *Rc* to be 0.25, because the EAR5 and YSU schemes use the same

177     method and threshold value when calculating PBLH (Hong et al., 2006; ECMWF, 2017).

178     CD, YB, DZ and CQ were selected as representative cities for analysis in the study. These four

179     representative cities are located in the western, southern, northwestern, and eastern regions of the basin,

180     to capture diverse pollution and meteorological conditions within the SCB. These cities were chosen to

181     represent the most polluted regions (Zhao et al., 2018; Lu et al., 2022), as well as typical basin and

182     mountainous cities. Furthermore, there are only four sounding stations in the SCB available, which are

183     located in these four representative cities. They can provide valuable vertical and surface

184     meteorological observations, as well as pollution data, contributing comprehensive dataset used in this

185     study.

186     ERA5 reanalysis data from the European Centre for Medium-Range Weather Forecasts (ECMWF),

187     which assimilates comprehensive observation data, including ground observation, sounding data,

188     aircraft observation data, and satellite observation data, were obtained for synoptic pattern

189     classification and their impact on meteorological factors in four representative cities. The EAR5

190     data at the 850 hPa pressure level were collected for the synoptic pattern study. Additionally, cloud

191     liquid water content and downward solar radiation derived from the EAR5 single–level datasets

192     were obtained to assess the influences of synoptic forcing on CRI studies, while PBLH were

193     adopted to conduct the simulation verification. Previous studies have demonstrated the reliability

194     of ERA5 data in estimating cloud properties, including the cloud liquid content (Yao et al., 2019;

195     Nandan et al., 2022; Ojo et al., 2023).

196     **2.2 Synoptic pattern classification**

197     The objective classification was conducted on the synoptic patterns of the SCB using ERA5 data,

198     including geopotential height, u, and v components of winds at the 850 hPa pressure level. The

199     analysis covered an area of 97–117° E and 24–37° N with a horizontal resolution of 0.25° × 0.25°.

200     Given that PM pollution in the SCB is primarily prevalent during winter months (Zhao et al., 2018;

201     Lu et al., 2022), the synoptic pattern classification was performed for winter seasons from 2015 to

202     2021 (December, January, and February) using the principal component analysis in the T–model

203     (T–PCA) objective method. Compared with the subjective classification method, the objective

204     method can process large amounts of data without relying on subjective experience (Huth et al.,

205     2008; Miao et al., 2017). Among various classification methods, the T–PCA method accurately

206 reflects the characteristics of the original synoptic circulations and exhibits spatial and temporal
207 stability (Huth et al., 1996; Huth et al., 2008). Consequently, the T–PCA has been widely used in
208 synoptic pattern classification researches (Ning et al., 2019; Miao et al., 2020; Li et al., 2021).

## 209 **2.3 Model configuration and simulation experiments**

210     To understand the combined effects of synoptic patterns and CRI inhibition on ARI and PBL, a
211 series of parallel experiments were conducted on the simulation of a typical pollution episode
212 using the Weather Research and Forecasting model with Chemistry (WRF–Chem v3.9.1) (Grell et
213 al., 2005). The Advanced Research WRF (ARW) dynamics solver integrates the compressible,
214 nonhydrostatic Euler equations, for example, the momentum equation, the continuity equation, the
215 thermodynamic equation, the moisture equation and the ideal-gas equation of state (Skamarock et
216 al., 2008). The model domain (Fig. 1a) was centered over the SCB and utilized three layers of
217 nested grids with horizontal resolutions of 27, 9, and 3 km, respectively. A total of 32 vertical
218 layers spanning from the surface to 100 hPa were defined. Initial and boundary meteorological fields
219 were obtained from the National Centers for Environmental Prediction Final reanalysis data with a
220 horizontal resolution of $1° \times 1°$ and 6 h time interval. For chemical process simulations,
221 anthropogenic emissions were sourced from the Multiresolution Emission Inventory for China
222 (MEIC) in 2016, featuring a grid resolution of $0.25° \times 0.25°$. To address the empirically
223 overestimated $PM_{2.5}$ emissions by the MEIC in the SCB (Zhan et al., 2023), the ensemble square
224 root Kalman filter were implemented on the $PM_{2.5}$ emission during simulation (Wu et al., 2018;
225 Lu et al., 2021). Biogenic emissions were calculated online using the Guenther scheme (Guenther
226 et al., 2006). Table 1 provides a summary of the chosen physical and chemical parameterization
227 schemes. The parameterization schemes employed in this study is the one used by the Chongqing
228 Meteorological Bureau in the daily operational activities. The schemes have been obtained
229 through multiple sets of control experiments and are considered suitable for the simulation in the
230 SCB.

231 **Table 1 The main options of WRF–Chem**

| Items | Contents |
|---|---|
| **Domains (x, y)** | (155, 110), (184, 160), (320, 250) |
| **Grid spacing (km)** | 27, 9, 3 |
| **Center** | (29.1° N, 106.2° E) |
| **Time step (s)** | 60 |
| **Microphysics** | WRF Single–Moment 5 class (WSM5) scheme |
| **Longwave radiation** | RRTMG scheme (Iacono et al., 2008) |
| **Shortwave radiation** | RRTMG scheme (Iacono et al., 2008) |
| **Planetary boundary layer** | Younsei University scheme (Hong et al., 2006) |
| **Land surface** | United Noah land surface model (Tewari et al., 2004) |
| **Cumulus parameterization** | Grell–Freitas ensemble scheme |

| | (Grell et al., 2013) |
| --- | --- |
| **Advection** | fifth- and third-order differencing for horizontal and vertical advection respectively |
| **Photolysis scheme** | Fast-J photolysis (Fast et al., 2006) |
| **Gas–phase chemistry** | RADM2 (Stockwell et al., 1990) |
| **Aerosol module** | MADE/SORGAM (Schell et al., 2001) |

232

233  To assess the impact of CRI inhibition on ARI under typical synoptic pollution patterns, four

234 parallel experiments were conducted using simulation models. The selected simulation period for

235 these experiments was January 1-7, 2017. The period was selected for two reasons: the Chinese

236 government announced clean-air action in the year of 2013, aiming to reduce $PM_{2.5}$ concentrations in

237 the next 5 year. Specifically, the year of 2017 was identified as a key year for assessing $PM_{2.5}$ pollution

238 in China, as significant  practical actions were implemented during the period (Wang et al., 2020) and

239 the selected period encompassed both typical pollution and clean weather patterns.

240  The baseline experiment (BASE) included both CRI and ARI in the simulations. In contrast, the

241 three sensitivity experiments focused on excluding either ARI or CRI. Experiment 1 (EXP1) did not

242 consider ARI, Experiment 2 (EXP2) did not include CRI, and Experiment 3 (EXP3) omitted ARI

243 when CRI was not included. The differences between BASE and EXP1 represented the

244 disturbances caused by ARI, while EXP2 and EXP3 represented the influences of ARI without

245 CRI inhibition. Detail differences between the experiments could be found in Table 2. The

246 numerical experiments were initiated at 00:00 UTC on December 30, 2016, and ran until 00:00

247 UTC on January 8, 2017, with the first 48 hours designated as a model spin–up period.

248 **Table 2 Four numerical simulation experiments are conducted in the study**

| Experiments | Description | Results | Meaning |
| --- | --- | --- | --- |
| **BASE** | Baseline simulation | BASE-EXP1 | Disturbances by ARI |
| **EXP1** | Only shutting down ARI | | |
| **EXP2** | Only shutting down CRI | EXP2-EXP3 | Influences of ARI without CRI |
| **EXP3** | Shutting down both ARI and CRI | | |

249        \*ARI: aerosol radiation interaction; CRI: cloud radiation interaction

250 **3 Results and discussions**

251 **3.1 Relationships between synoptic patterns and $PM_{2.5}$ pollution in the SCB**

252  Figure 2 illustrates the daily mean variations in $PM_{2.5}$ concentration and vertical distributions

253 of potential temperature (PT) during winter period from 2015 to 2021, with a focus on the pollution

254 episodes. The four sounding stations located in separate areas of the SCB (CD, YB, CQ, and DZ),

255 consistently experienced pollution processes characterized by simultaneous changes in vertical

256 thermal structures. For example, during the pollution events in January 2017 and December 2020,

257 the PM$_{2.5}$ concentrations in all four cities reached their peak levels at the same time before rapid

258 declining (Fig. 2). Interestingly, these pollution episodes were accompanied by warming in the

259 upper layer atmosphere, while a decrease in PM$_{2.5}$ concentration correlated with cooling. Despite

260 the significant distances between these cities (approximately 200–400 km), the synchronized

261 changes in pollutant concentrations and vertical thermal structures could be attributed to large–

262 scale synoptic patterns (Miao et al., 2020; Li et al., 2021). While the four cities with sounding

263 stations were selected as representatives for vertical thermal structure analysis, other cities in the

264 SCB also experienced pollution episodes and relevant physical processes, except for GY (Fig. S1).

265 GY is located in the northern edge of the SCB, bordering Shaanxi and Gansu Provinces. The proportion

266 of heavy PM$_{2.5}$ pollution in GY is the lowest in the basin, but the proportion of PM$_{10}$ pollution is higher

267 than other cities of SCB (Lu et al., 2022). Due to the lower PM$_{2.5}$ concentration, the two pollution

268 processes in January 2017 in GY were not as significant as in other cities whithin the basin. However,

269 the warming of upper air coincided with PM$_{2.5}$ increase could still be observed.
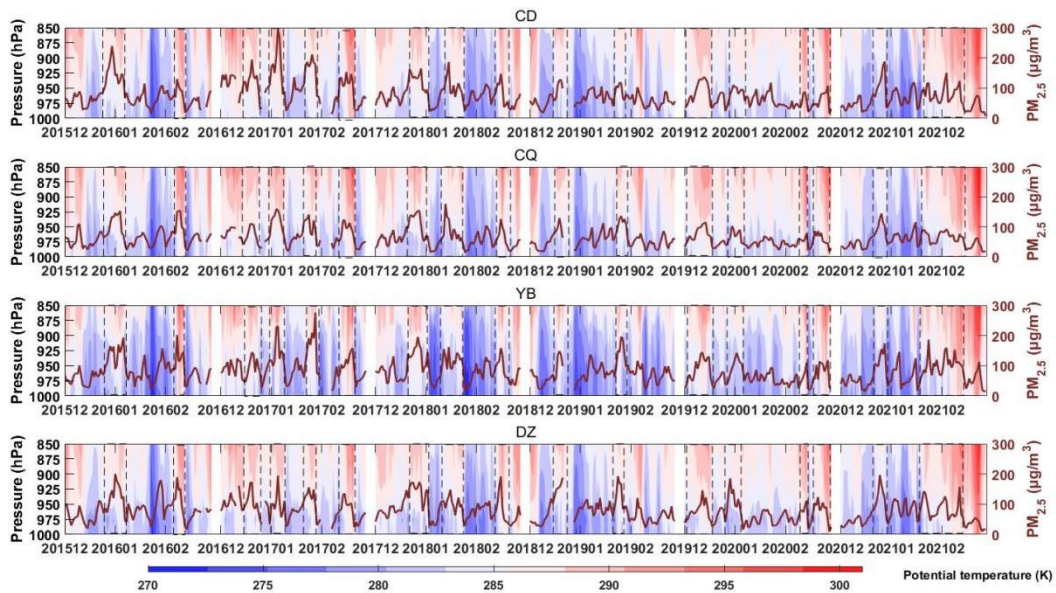
**Figure 2.** Time series of daily mean PM$_{2.5}$ and potential temperature derived from the sounding data during 2015-2021 winter months. The PM$_{2.5}$ pollution episodes are marked with black dotted boxes.

270

271    The time series of daily mean PM$_{2.5}$ from air quality monitoring sites and the accompanying

272 vertical distributions of temperature, relative humidity, and wind in CD, CQ, YB, and DZ derived from

273 the sounding stations are shown in Fig. S2, focusing on January 2017 as an example for analysis.

274 During this month, two severe PM$_{2.5}$ pollution episodes occurred: one from January 1 to 7 and another

275 from January 24 to 31 in 2017. These pollution episodes had a significant impact on air quality in all

276 four cities. The highest daily PM$_{2.5}$ concentrations recorded during these episodes were 291.17 μg/m$^3$ in

277 CD and 276.2 μg/m$^3$ in YB. Pollution in early January exhibited a gradual increase in PM$_{2.5}$ levels from

278 January 1 to 3, with upper air warming and the emergence of an inversion above the PBL. Additionally,

279 lower humidity and higher wind speeds above 1500 m were observed during the pollution

280 accumulation period. Similarly, the late January pollution episode showed a rapid increase in PM$_{2.5}$,

281 from January 24 to 27, together with warming, dryness, and high wind speed above 1500 m in all four

282 cities. These consistent meteorological conditions during the pollution periods indicated significant
283 synoptic forcing. The previous study has found that winter heavy pollution processes in the SCB are
284 usually associated with abnormal warming above the 850 hPa (Lu et al., 2022). The warming is
285 induced by strong southerly airflow above the basin. The southerly airflow in winter over the SCB
286 originates from the Yunnan-Guizhou Plateau or the Indian Peninsula, characterized with high
287 temperature, dryness, and high wind speed. The strong southerly airflow forms a warm lid over the
288 basin, suppressing the vertical exchange of pollutants within the basin. As a result, pollutants
289 accumulate rapidly, which may explain the phenomenon of rapid $PM_{2.5}$ growth accompanied by
290 warming, dryness, and strong winds above 1500 m. Notably, the key layer for studying the connection
291 between synoptic patterns and $PM_{2.5}$ pollution is approximately 850 hPa, corresponding to a height of
292 approximately 1500 m within the PBL, where changes in specific meteorological conditions primarily
293 affect surface–emitted pollutants.

294 Using ERA5 reanalysis data for winter (December, January, and February) from 2015 to 2021,
295 the 850 hPa synoptic patterns over the SCB were objectively classified into six types (Fig. 3).
296 According to the relative positions of the high–pressure and low–pressure systems in the basin,
297 these synoptic patterns could be described as follows: (1) strong high pressure in the north, (2) east
298 high west low (EHWL) pressure, (3) weak high pressure in the north, (4) weak ridge of high
299 pressure after the trough, (5) low trough (LT), and (6) strong high pressure. Patterns 1 and 3
300 exhibited high pressure in the northern SCB, which differed from the high–pressure intensity. With
301 strong high pressure, the basin was primarily controlled by northerly airflow. Under weak high–
302 pressure conditions, the basin was dominated by an easterly backflow. Patterns 2 and 5 had high
303 and low pressures near the basin, forming a relatively dense isopotential altitude gradient and
304 resulting in strong southerly winds over 850 hPa. Pattern 4 was a weak high–pressure ridge after a
305 trough controlled the SCB with sparse isobaric lines and weak winds leading to static and stable
306 weather conditions. During Pattern 6, the SCB was controlled by the cold high-pressure system,
307 accompanying weak northerly airflow on the basin. Pattern 6 usually evolved from either Pattern 1
308 or Pattern 3.
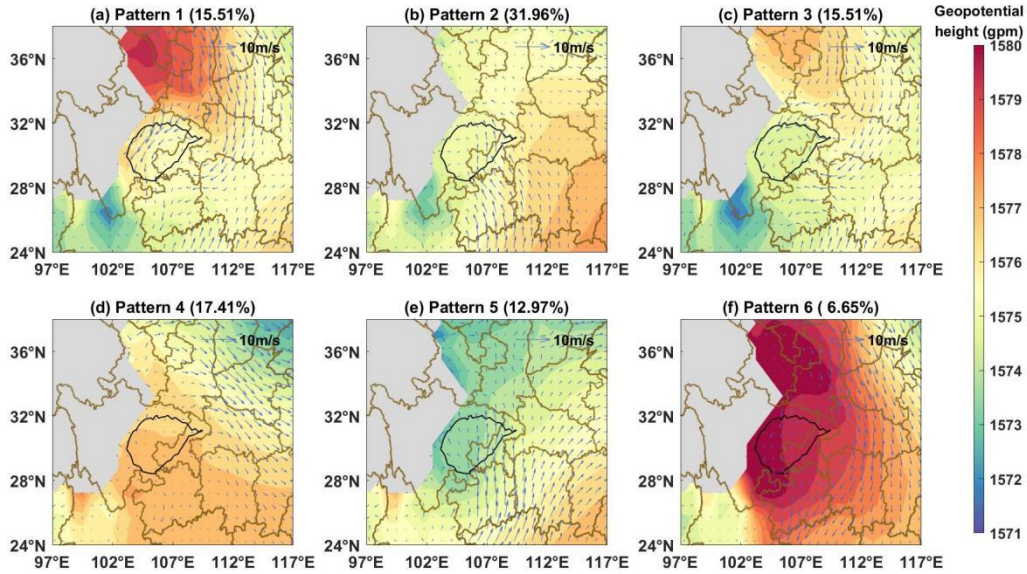
**Figure 3.** The 850hPa geopotential height field (shading) with wind vector fields (blue vectors), and frequency of occurrence for 6 synoptic patterns during 2015-2021 winter months. The SCB was outlined with an altitude contour of 750 m terrain height (black lines).

309

310  Patterns 2, 4, and 5 exhibited higher frequencies of pollution occurrence ($PM_{2.5}$ daily

311 concentration ≥ 75 μg/m³) according to statistical results from 18 cities in the SCB during the

312 2015–2021 winters (Fig. 4a). These patterns were associated with high $PM_{2.5}$ concentrations in 50–

313 70 % days, including CD, DY, and MY in the northern SCB, 40–60 % for cities in the southern

314 SCB, such as ZG and YB, and also 40–60 % of days for cities in the northern SCB, such as CQ, DZ,

315 NC, and GA. Furthermore, the average $PM_{2.5}$ concentrations in the respective cities for the six

316 synaptic patterns were calculated (Fig. 4b), aligning with the frequency of pollution occurrence.

317 The days under Patterns 2, 4, and 5 exhibited higher average daily $PM_{2.5}$ concentrations. The average

318 concentrations under these three synoptic patterns were 99.19, 103.43, and 111.97 μg/m³ for CD,

319 95.44, 87.98, and 94.26 μg/m³ for YB, 79.14, 83.96, and 74.77 μg/m³ for CQ, and 91.02, 104.64,

320 and 91.51 μg/m³ for DZ, respectively. Regarding the impact of synoptic patterns on the

321 accumulation or dispersion of $PM_{2.5}$, Fig. 4c illustrates the average daily changes in $PM_{2.5}$

322 concentration compared with the previous day for CD, CQ, YB, and DZ under the six synoptic

323 patterns. Patterns 2 and 5 exhibited the most significant $PM_{2.5}$ accumulation under the influence of

324 southerly airflow. The average $PM_{2.5}$ concentration under Pattern 1, 3 and 6 was lower in all cities

325 of SCB than other three pollution patterns (Fig. 4a). Besides, the day to day $PM_{2.5}$ variations under

326 Pattern 1, 3 and 6 exhibited negative growth trend in the four representative cities (Fig. 4c). As a

327 result, Pattern 1,3 and 6 were identified as the "clean pattern". In addition, the pollution

328 occurrence frequency of which was found higher for cities located in the eastern part of the SCB

329 than other parts. Under Pattern 6, strongest northerly airflow affects the basin. The eastern part of

330 the basin consists of parallel ridges and valleys, which reduces wind speed. The stronger the wind

331 is, the more obvious the reduction of wind by terrain is. In contrast, the western part is relatively

332 flat, which can result in higher surface wind speeds. The difference in wind impacted by terrain

led to a weaker pollution removal effect in the eastern region, thus contributing to a higher proportion of pollution days under Pattern 6. Besides, differences in precipitation rates between eastern cities and other regions were not significant (the proportion of rainfall with a daily accumulated precipitation exceeding 10 mm in CD, CQ, YB and DZ under Pattern 6 were all less than 3%) , which might not the main reason why eastern cities in the SCB experience higher pollution frequency.
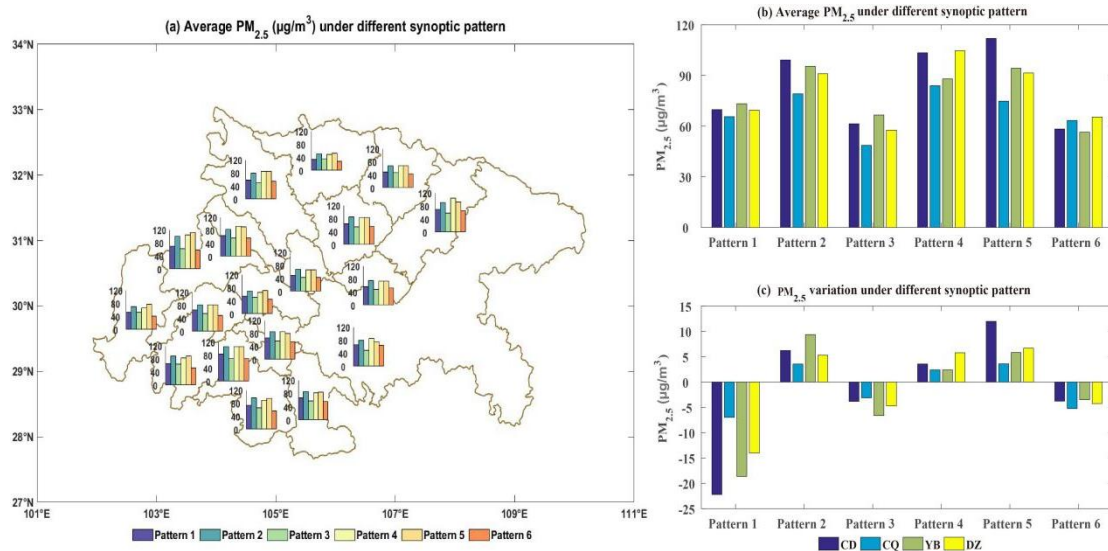
**Figure 4.** (a) The pollution occurrence frequency at 18 air pollution stations in SCB, (b) (c) average $PM_{2.5}$ concentrations and $PM_{2.5}$ day to day variations at 4 representative SCB cities, under 6 synoptic patterns.

The time series of daily mean $PM_{2.5}$ and the day-to-day classification of 850 hPa synoptic patterns are shown in Fig. S3, from December 2016 to January 2017. Six pollution episodes occurred during this period (December 03–12 and 16–26, 2016; January 1–7, 16–19, and 20–28, 2017; and February 14–23). It is observed that pollution episodes consistently began with Pattern 2 and ended with Pattern 1, accompanied by a rapid decline in $PM_{2.5}$. This finding suggests that Pattern 2 acted as a key synoptic forcing for the initation of pollution episodes. Additionally, statistical results revealed that Pattern 2 accounted for a high proportion of $PM_{2.5}$ increase during the six pollution episodes, reaching 48.48 %, while Pattern 5 had the second highest proportion of 21.88 %, with Patterns 2 and 5 combined accounting for more than 70 % of the pollution episodes. For example, during the two heavy pollution events in early and late January 2017, $PM_{2.5}$ rapidly accumulated with the interplay of Patterns 2 and 5. These two patterns represented a substantial proportion of 31.96 % and 12.97 %, respectively, during winters from 2015 to 2020 at 850 hPa level in the SCB (Fig. 3). Based on this analysis, Patterns 2, 4, and 5 were identified as synoptic pollution patterns, whereas Patterns 1, 3, and 6 were as clean patterns. In summary, Patterns 2 and 5 played crucial roles in the initiation and accumulation of $PM_{2.5}$ during pollution episodes.

The discussion above showed that pollution in the SCB tended to occur when southerly airflow controlled the upper-layer of the basin (Pattern 2 and 5), while the dispersion of pollutants was

357 accompanied by northerly winds, which aligns with the findings of Lu et al. (2022). This study
358 indicated that southerly airflow in the upper-layer could bring warm air, leading to warming above
359 the basin and forming a "warm lid". The surrounding mountains and plateau with the "warm lid"
360 contributed to the formation of a relative enclosed space within the SCB, facilitating local
361 circulations and allowing for the thorough mixing and secondary reactions of local emission and
362 pollutants transported from outside. As a result, persistent and severe pollution often occurred
363 under the influence of southerly airflow. When the northerly airflow began to dominate the SCB,
364 the "warm lid" and local circulation were disrupted, leading to dispersion of pollutants through
365 advection and vertical transport. Northerly winds were often associated with cold air and
366 sometimes accompanied by weak precipitation, resulting to wet deposition and the removal of
367 pollutants. Therefore, the arrival of northerly airflow often signified the ending of the pollution
368 episode. The evolution of 850 hPa synoptic forcing and vertical meteorological conditions (Fig. 2
369 and 6) aligns with the study of Lu et al (2022). Therefore, there are also similar pollution change
370 mechanisms.

371 Due to the convergence of air moving eastward across the Tibetan Plateau, the SCB experiences
372 frequent wet and cloudy weather, with cloud cover fraction exceeding 80 % (Yu et al., 2004;
373 Zhang and Lin, 1985). Clouds undoubtedly play an unneglectable role in the interactions of
374 aerosols, radiation, and the PBL under typical synoptic forcing in this region. This study evaluated
375 the average cloud liquid water content, downward solar radiation, and PBL under the influence of
376 the six classified synoptic patterns in CD, CQ, DZ, and YB, using data from ERA5 (Fig. 5). The
377 reanalysis data revealed significant higher cloud liquid water contents with Patterns 2 and 5, likely
378 triggered by robust southerly air prevailing at 850 hPa over the SCB (Fig. 3). This southerly air
379 brought warm and moist air, contributing to cloud formation. Dense clouds reduced solar radiation
380 through reflection and scattering, resulting in surface cooling and inhibiting PBL development.
381 The PBLH under Patterns 2 and 5 was approximately 900–1000 m, lower than that under the
382 influence of clean synoptic Pattern 6 at 1500 m or Pattern 1 and 3 at 1200–1300 m (Fig. 5). In
383 contrast, the clean synoptic Pattern 1 was characterized by a strong northerly flow at 850 hPa,
384 resulting in lower cloud liquid water content over the basin and increased solar radiation, promoting
385 PBL development. The lower PBLH with more stable stratification caused by the CRI in Patterns 2
386 and 5 could partially explain the rapid accumulation of $PM_{2.5}$ during these two pollution patterns.
387
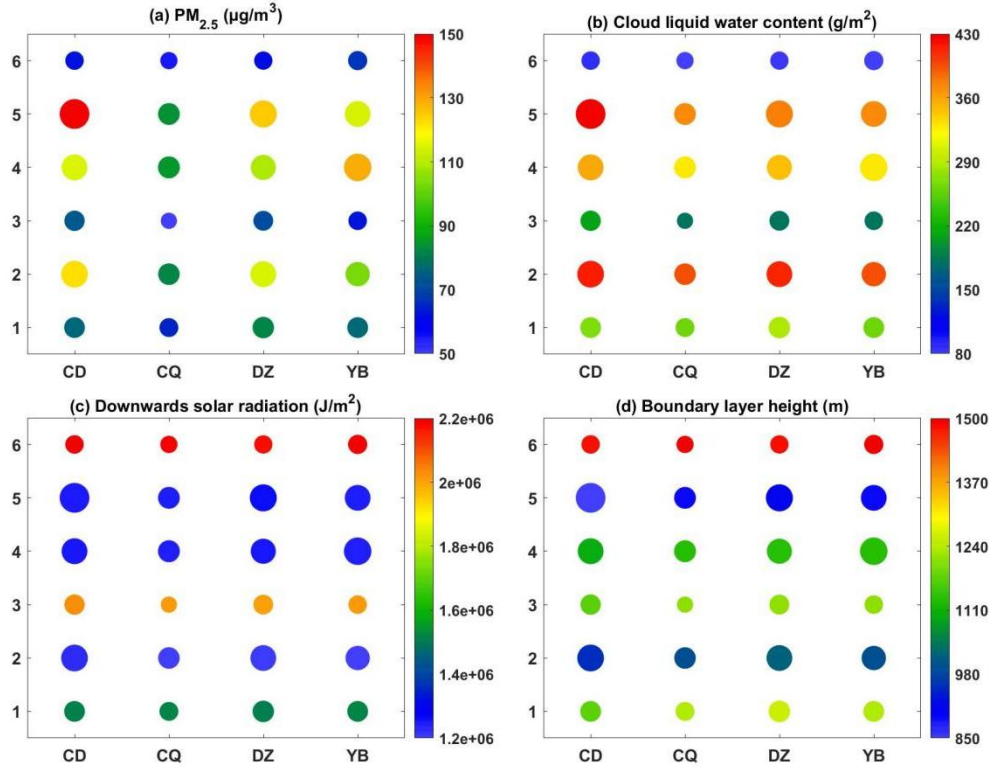
**Figure 5.** The averaged (a) PM₂.₅ concentrations, (b) cloud liquid water contents, (c) downwards solar radiation and (d) boundary layer height derived from 2015-2021 winter months ERA5 reanalysis data, at 4 representative SCB cities under 6 synoptic patterns, the dot sizes represent PM₂.₅ concentrations.

388

### 3.2 Integrate impacts of synoptic patterns and the CRI inhibition on ARI

390    Based on the above analysis, Patterns 2 and 5 were identified as the key pollution synoptic
391    patterns accompanying dense clouds and, thus, strong CRI. However, the effects of pollution
392    patterns on ARI and their interaction with CRI in the SCB remain unclear and warrant further
393    investigation. A typical pollution episode from January 1–7, 2017, was selected to understand these
394    complex processes and simulated using WRF–Chem. The BASE simulations were verified with
395    observations to determine the accuracy and reliability of the simulation results. The simulation and
396    observation of PM₂.₅, T2, TD2 and wind speed values with some statistical metrics in CD from
397    January 1–7 are shown in Fig. 6a-d. Similar information at CQ, YB and DZ can be found in the
398    Fig. S4. The MB of the simulated and observed PM₂.₅ concentrations were -15.59, -13.42, 2.10
399    and -13.11 μg/m³, with NMB values of -4.12%, -4.22%, 6.01% and -0.68% at four cities,
400    respectively, which are within the acceptable standards (NMB < ± 15%). The R of PM₂.₅ were
401    78.91%, 57.23%, 61.15% and 62.86% for four representative cities, respectively. The statistical
402    metrics for PM₂.₅ are consistent with previous studies (Wang et al., 2020; Shu et al., 2021; Zhan et
403    al., 2023), indicating that our model results for PM₂.₅ are reasonable and acceptable. Regarding to
404    the surface meteorological factors, low MB and high R for both temperature and dew point

temperature suggested good simulation performance for these variables. However, the simulation results for wind speed were poor, which was expected under conditions of low wind and complex terrain. The high observed calm wind frequency, influenced by the starting speed of the anemometer, led to an overestimation in the simulation (Shu et al., 2021; Zhan et al., 2023). Additionally, it could be argued that unresolved topographic features introduce additional drag, beyond that generated by vegetation, which was not considered in the WRF model (Jimenez and Dudhia, 2012).

In addition, the temporal averaged and variations of vertical profiles for potential temperature, relative humidity and wind speed in the model were compared with the sounding data in CD (Fig. 6e-m). Model evaluation of vertical structures in CQ, YB and DZ can be found in Fig. S5. The SCB is characterized with cloudy and foggy conditions, which result in abundant water vapor and near 100% relative humidity above the nocturnal boundary layer. Models often underestimate the humidity above the boundary layer during night in the SCB (Shu et al., 2021). Furthermore, due to complex terrain and measurement bias of the anemometer for weak winds, the evaluation of simulation results for wind speed often exhibit certain deviations (Jimenez and Dudhia, 2021; Shu et al., 2021; Zhan et al., 2023). For the verification of PBLH, sounding data are commonly regarded as reliable vertical observation records, and PBLH calculated based on sounding data can be used as the true values to compare with other data for long-term validation (Guo et al., 2016). However, for short-term studies, due to limited availability of sounding data at only 00:00 and 12:00 UTC, the ERA5 data were also incorporated for the model evaluation of PBLH in this study (Fig. 6 and Fig.S5). The simulation PBLH showed a consistent trend with those calculated from ERA5 and sounding data. Overall, the simulation results can capture the meteorological and $PM_{2.5}$ variation trends. According to the simulation evaluation standards for the SCB in previous studies (Wang et al., 2020; Zhan et al., 2023), the results is acceptable and reasonable; thus, the simulation can be used for subsequent analysis and discussion.
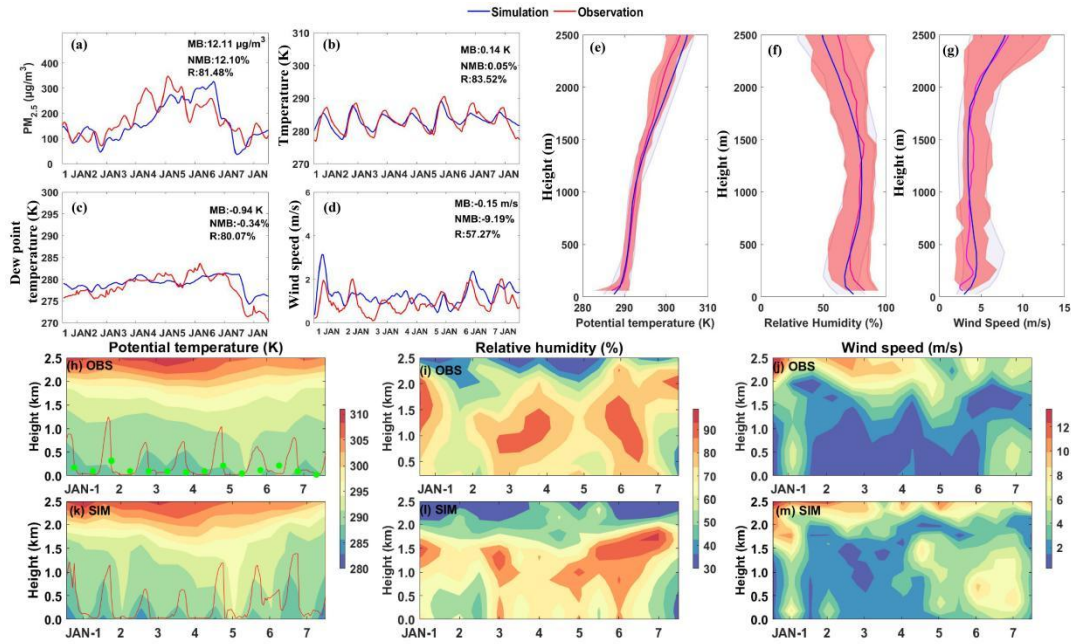
**Figure 6.** Time series of hourly simulated and observed (a) PM₂.₅ concentration, (b) temperature at 2 m, (c) dew temperature at 2m and (d) wind speed near surface, and comparison of simulated and observed mean vertical profile of (e) potential temperature, (f) relative humidiy and (g) wind speed, the red and grey shaded areas represent deviations to the mean values of observation and simulation, respectively. The simulated and observed time-height sections of (h)(k) potential temperature, (i)(l) relative humidity and (j)(m) wind speed are also given, while the red lines in (h)(k) are time series the boundary layer heights derived from ERA5 data and simulation with green dots representing boundary layer heights calculated with sounding data. The above figures display information in CD. Additionally, the model verification information regarding CQ, YB and DZ can be found in Supplement Figure 3 and 4.

429

430    During the pollution episode that occurred from January 1 to 7, 2017, the pollution synoptic
431 patterns controlled the SCB as follows: Pattern 2 from January 1 to 3, Pattern 5 from January 4 to 6,
432 and Pattern 1 on January 7. Consequently, PM₂.₅ pollution in the SCB occurred on January 1–6 and
433 rapidly dissipated on January 7 (Fig. 7). The mean geopotential height at 850 hPa derived from the
434 simulation of January 1–3 under Pattern 2 showed EHWL, with southerly flow prevailing over the
435 SCB (Fig. 7a). The resulting upper air warming suppressed PBL development (Fig. 7d). During
436 January 1–3 under Pattern 2, the average PBL heights were lower (Fig. 7d), acting as a lid above the
437 SCB and hindering the airflow within the basin due to the surrounding mountains. Low wind
438 speeds provided adverse diffusion conditions for pollutants emitted into the basin, resulting in
439 severe pollution in the western and southern SCB (Fig. 7g). From January 4 to 6, the low pressure
440 over the SCB evolved into a LT pattern, termed Pattern 5 in the previous analysis. Compared with
441 Pattern 2, the isobaric lines were denser under the influence of the LT, leading to stronger southerly
442 winds above the SCB (Fig. 7a–b). Lower average PBL heights were observed during January 4–6

443 under Pattern 5 compared with those of January 1–3 under Pattern 2 (Fig 7d–e), primarily due to
444 stronger upper air warming and more stable stratification. Pollutants that accumulated during
445 January 4–6 from the earlier pollution episode (January 1–3) further increased (Fig. 7g–i). On
446 January 7, high pressure in the north dominated the SCB, with a prevailing northerly flow over the
447 basin (Fig. 7c). The PBL height quickly increased due to upper-layer cold advection (Fig. 7f),
448 resulting in a rapid decrease in PM$_{2.5}$ (Fig. 7i). Overall, synoptic patterns play a key role in the
449 accumulation and diffusion of PM$_{2.5}$ during pollution episodes by modulating PBL development
450 and stratification stability.
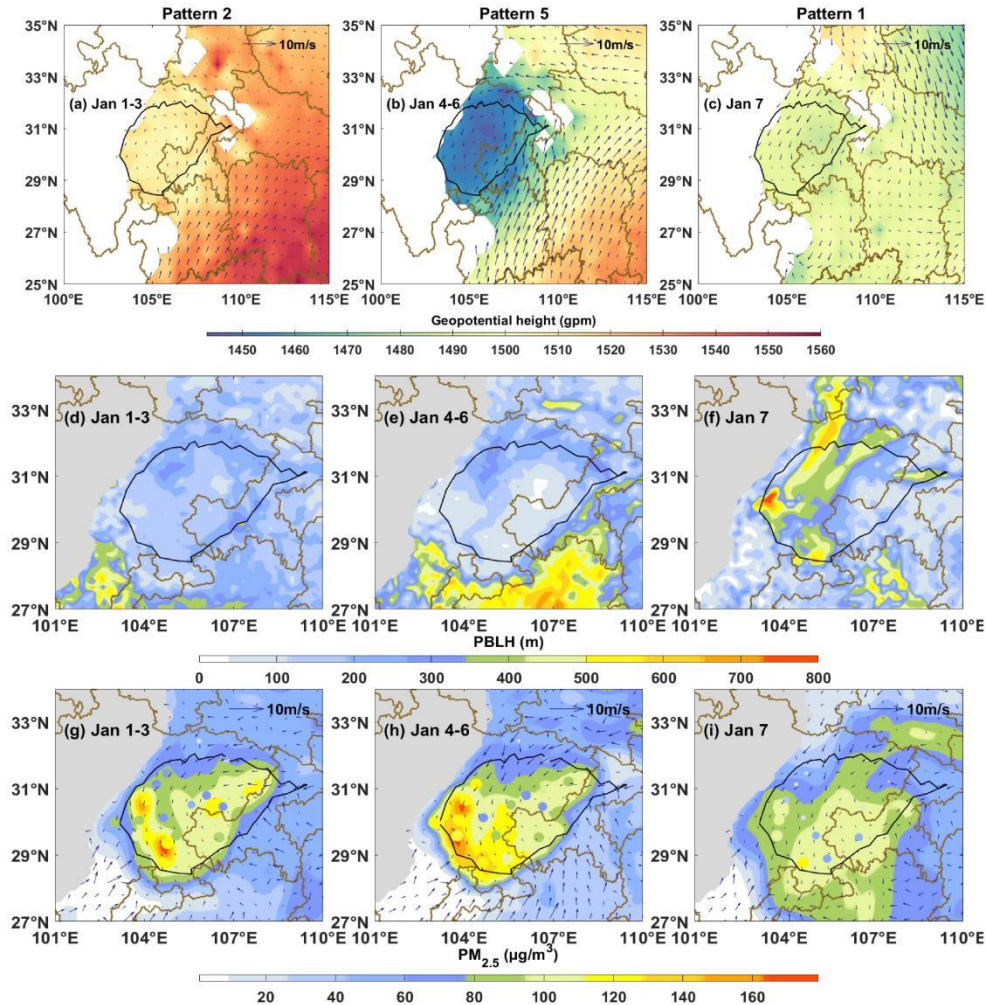
**Figure 7.** The simulated (a)-(c) 850 hPa geopotential height field (shading) with wind vector fields (blue vectors), (d)-(f) boundary layer height and (g)-(i) PM$_{2.5}$ concentrations (shading) and wind vector fields at 900hPa (blue vectors) for 1-3, 4-6 and 7 January. The size and color of scatters in (g)-(i) show corresponding observed PM$_{2.5}$ concentrations at 18 air quality monitoring stations. The SCB was outlined with an altitude contour of 750 m terrain height (black lines).

451

452 Pollutant accumulation can regulate the PBL structure through the ARI, further exacerbating
453 pollution (Wang et al., 2018; Miao et al., 2020). In the SCB, this positive feedback is weaker than
454 in the other regions and may be inhibited by cloud radiation (Zhong et al., 2019). A series of
455 simulation experiments were conducted to investigate the aerosol radiation feedback in the SCB

under the influence of two typical synoptic pollution patterns, as described in Section 2.4. BASE–EXP1 represents the perturbations caused by ARI, whereas EXP2–EXP3 demonstrates changes through ARI without CRI inhibition. Aerosols led to surface cooling through absorbing and scattering solar radiation, thereby inhibiting the development of the PBL, which in turn facilitated pollutant accumulation (Fig. 8). Compared with Pattern 2, the aerosol concentrations in Pattern 5 were higher, resulting in greater reduction of downward solar radiation reduction due to ARI, leading to more pronounced cooling near the ground and a lower PBLH. Overall, the ARI in Pattern 5 was more significant than that in Pattern 2, regardless of CRI inhibition (Fig. 8).
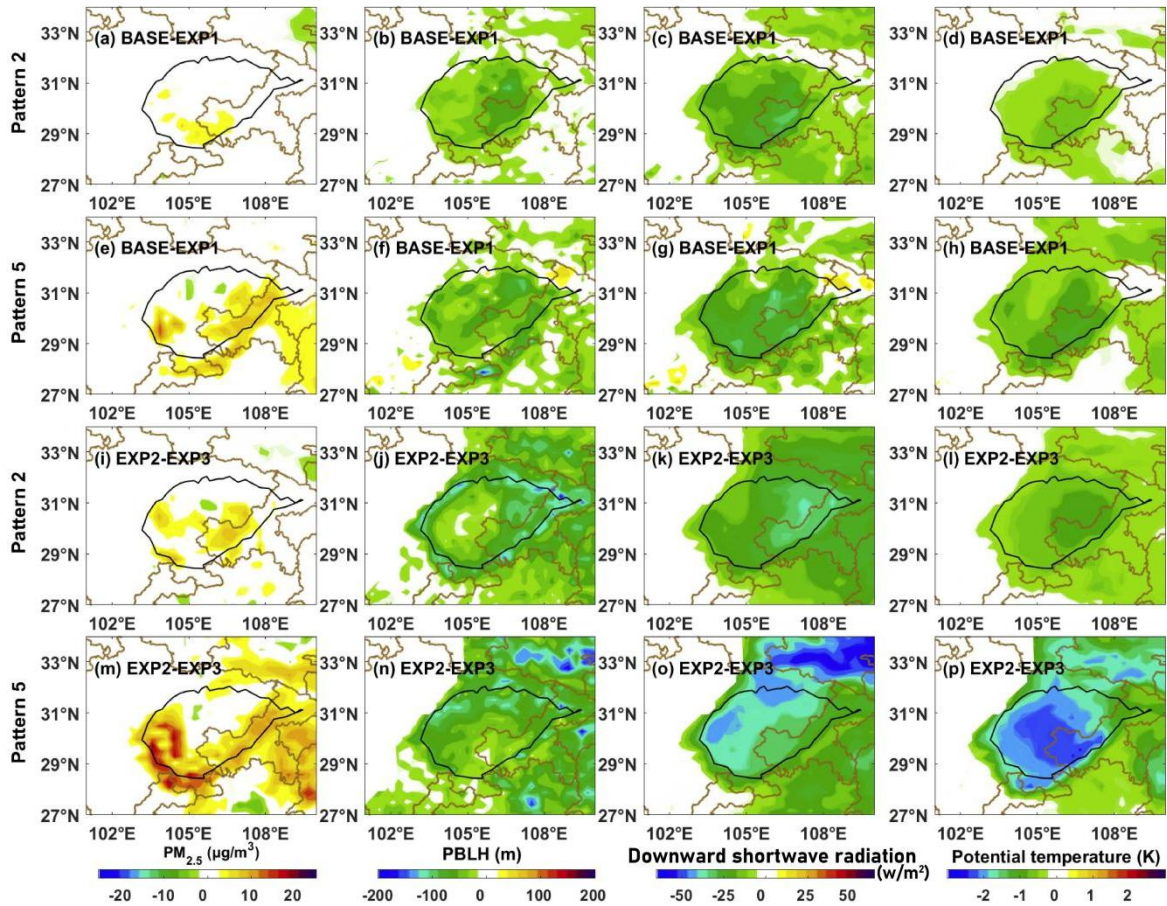
**Figure 8.** Spatial distribution of perturbations induced by (a)-(h) aerosol radiation interactions (ARI), and (i)-(p) ARI without the cloud radiation interaction (CRI) inhibition during 1-3 and 4-6 January representing Pattern 2 and Pattern 5 synoptic forcing, respectively. The SCB was outlined with an altitude contour of 750 m terrain height (black lines).

Furthermore, parallel simulation experiments revealed that the CRI significantly attenuated the ARI in the SCB under both pollution synoptic patterns. When the CRI was not considered, more solar radiation penetrated the PBL. Dense aerosols accumulated near the surface, intercepting more downward shortwave radiation, and resulting in stronger cooling near the ground. This suppressed the development of the PBL, and contributed to a more remarkable ARI (Fig. 8). Regarding the horizontal spatial distribution, a strong ARI was primarily observed in CQ, as well as in the western and southern SCB, despite CQ experiencing lower pollutant concentrations compared to the other

472     two regions (Figs. S4 and 7). This weaker ARI phenomenon in the western SCB was also reported

473     by Zhong et al. (2019) and was attributed to CRI inhibition on ARI. Considering the statistical

474     results in Fig. 5, the average cloud liquid water content in CD and YB was significantly higher than

475     that in CQ under the influence of Patterns 2 and 5. Consequently, a more remarkable CRI

476     inhibition on the ARI would occur in the western and southern SCB compared to CQ, leading to a

477     relatively weaker ARI distribution in these regions. Without considering the CRI, the ARI in the

478     western and southern SCB would be much more pronounced than that in CQ. As for the

479     northwestern SCB (DZ), the ARI in DZ is lower than in the other three regions. When the CRI is not

480     considered, the ARI in DZ is higher than in CQ but lower than in CD and YB. This is because DZ has

481     lower aerosol concentrations compared to CD and YB (Fig. 7), but exhibits higher cloud cover than CQ

482     under Patterns 2 and 5 (Fig. 5).

483       Using the western SCB, which exhibited the highest pollution concentration, as an example, Fig.

484     9 illustrates the vertical diurnal variations in temperature and solar radiation caused by the ARI.

485     The results in Fig. 9–11 were derived from the simulation experiments in CD, as CD is one of the

486     most polluted cities with typical meteorological and geographical characteristics of the western SCB.

487     The ARI caused surface cooling in the morning and upper–air warming in the afternoon. As local

488     solar radiation increased from 8 am to 12 pm, the reduction in solar radiation caused by the ARI

489     also increased. Surface cooling reached its peak at approximately 10 am to 12 pm, and gradually

490     weakened in the afternoon. This diurnal variation might be attributed to the enhanced turbulence

491     during morning PBL evolution (Wang et al., 2018). Afternoon surface cooling was partly

492     compensated by the turbulent transport of warm air above the PBL. In addition, strong surface

493     cooling between 5 pm and 8 pm in the SCB, was possibly influenced by remarkable valley wind

494     circulations forced by the Qinghai–Tibet Plateau adjacent to the western SCB (Lu et al., 2022).

495     The evening cooling of the plateau induced strong mountain winds, promoting surface cooling,

496     while the upper–layer warming mainly occured around 1–1.5 km in the afternoon. In general, the

497     ARI reduces solar radiation, causing surface cooling and upper air warming, thereby regulating the

498     vertical atmospheric thermal structure, suppressing convection, and consequently decreasing PBL

499     heights (Fig. 10).
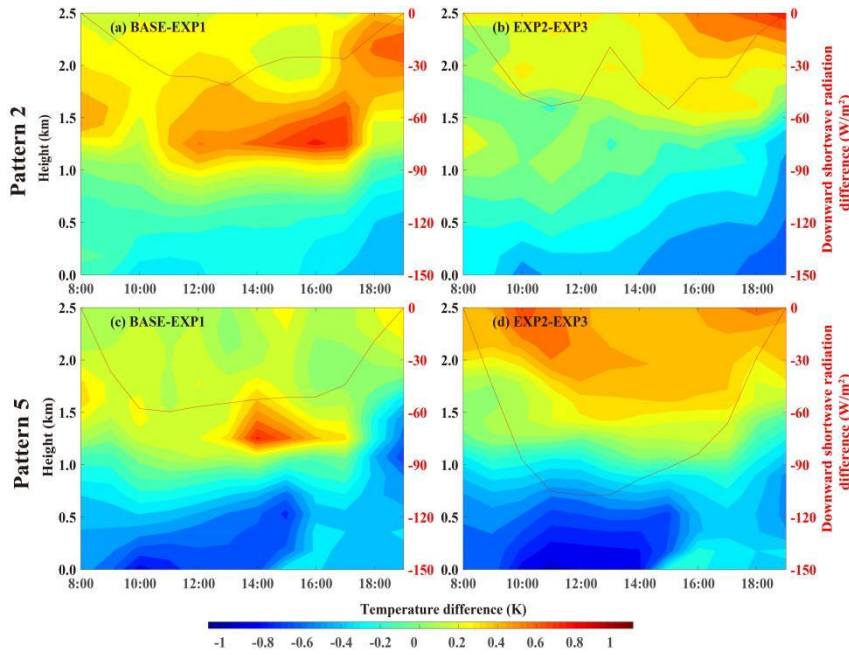
**Figure 9**. Diurnal variations of vertical temperature perturbations and downward solar radiation under influences of Pattern 2 and Pattern 5 induced by (a) (c) ARI and (b) (d) ARI without CRI inhibition.

500
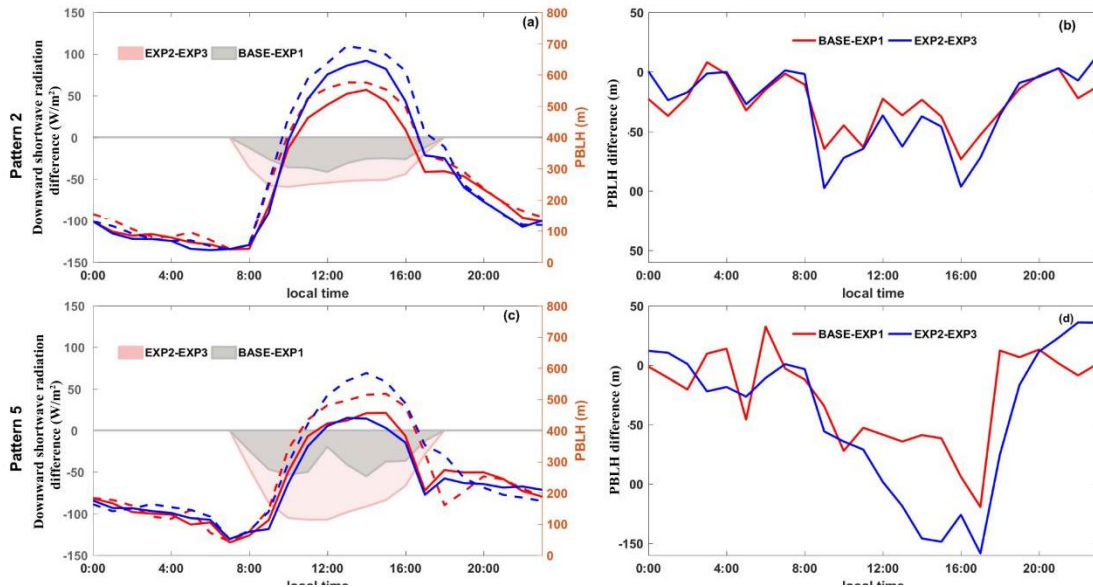
**Figure 10**. Diurnal variations of (a) (c) boundary layer height(lines) and downward solar radiation(shading), and (b)(d)the perturbations of boundary layer height induced by ARI and ARI without CRI inhibition, under Pattern 2 and Pattern 5 synoptic forcing respectively.

501
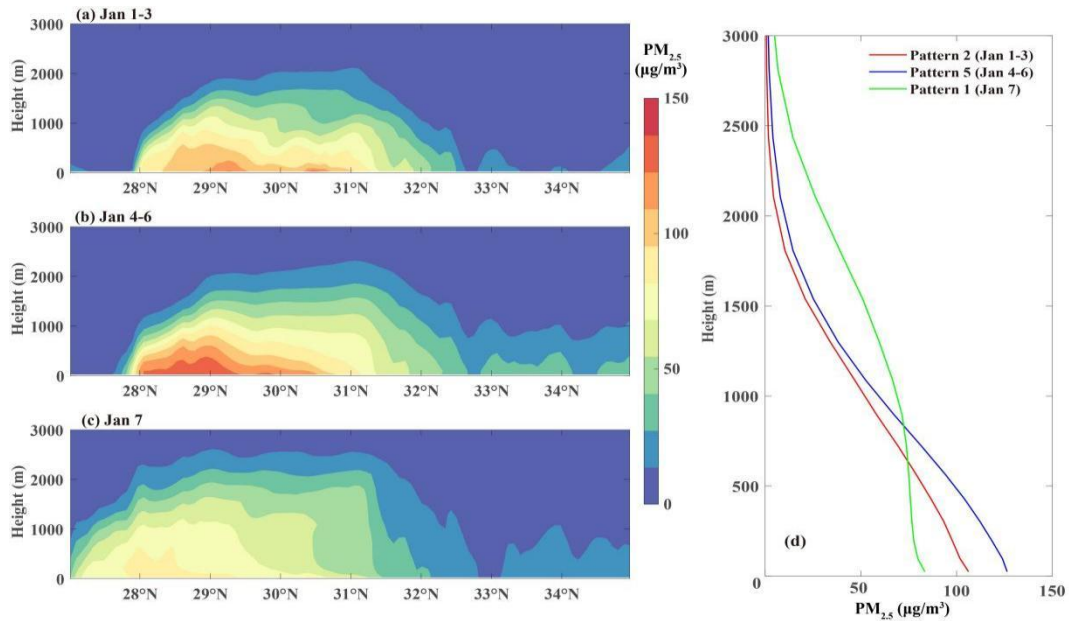
**Figure 11.** Meridional vertical distribution of averaged PM$_{2.5}$ between 104°E and 105°E under (a) Pattern 2 and (b) Pattern 5, and (c) average profiles of PM$_{2.5}$ within 28°N and 31°N.

Synoptic patterns play a role in the interaction between the ARI and PBL (Wang et al., 2018; Miao et al., 2020). Zonal average of PM$_{2.5}$ concentration between 104°E and 105°E was conducted, and the meridional vertical distribution of PM$_{2.5}$ between 27°N and 35°N was illustrated in Fig. 11a-b. Fig. 11(c) provides an average of PM$_{2.5}$ concentration within 28°N and 31°N, showing the vertical distribution profiles under Pattern 2 and 5. Due to the inhibition of "warm lid" above the SCB, the vertical exchange was not prominent under both Pattern 2 and 5, and PM$_{2.5}$ was more concentrated at the middle and lower levels. The PM$_{2.5}$ concentration under Pattern 5 was higher than Pattern 2 throughout the atmospheric column, indicating stronger aerosol radiative forcing and a more significant impact on the boundary layer structure under Pattern 5. During January 4–6, the surface cooling reached 1 K, with cooling layers higher than those observed on January 1–3. The differences in thermal structure modulations contributed to a lower diurnal PBLH in Pattern 5 than in Pattern 2 (Figs. 10a and c), indicating that Pattern 5 was more conducive to ARI. Based on the simulation experiments, this study further discussed the impact of synoptic forcing on the CRI inhibition of ARI. When the CRI was not considered, the solar radiation reduction at noon on January 4–6 by the ARI was nearly twice as high as when the CRI was considered. Correspondingly, surface cooling at noon was remarkably enhanced. In the evening, surface cooling occurred earlier and was stronger without the CRI (Fig. 9). The regulation of CRI on ARI was further reflected in changes in PBLH. Without the CRI, the diurnal PBLH increased significantly, with the PBLH decreased more with ARI without CRI inhibition. The PBLHs were decreased by the ARI during January 13–17 afternoon, reaching 2–3 times the decrease observed with CRI inhibition (Fig. 10). More significant CRI inhibition of ARI was revealed under Pattern 5 compared with that under Pattern 2, owing to the stronger ARI itself with higher aerosol

525  concentrations in Pattern 5 and the more apparent CRI inhibition with denser cloud liquid water
526  contents under the LT pattern (Fig. 5). Therefore, the intensity of CRI inhibition of ARI in the
527  SCB was altered by synoptic forcing, with stronger effects under the influence of LT.
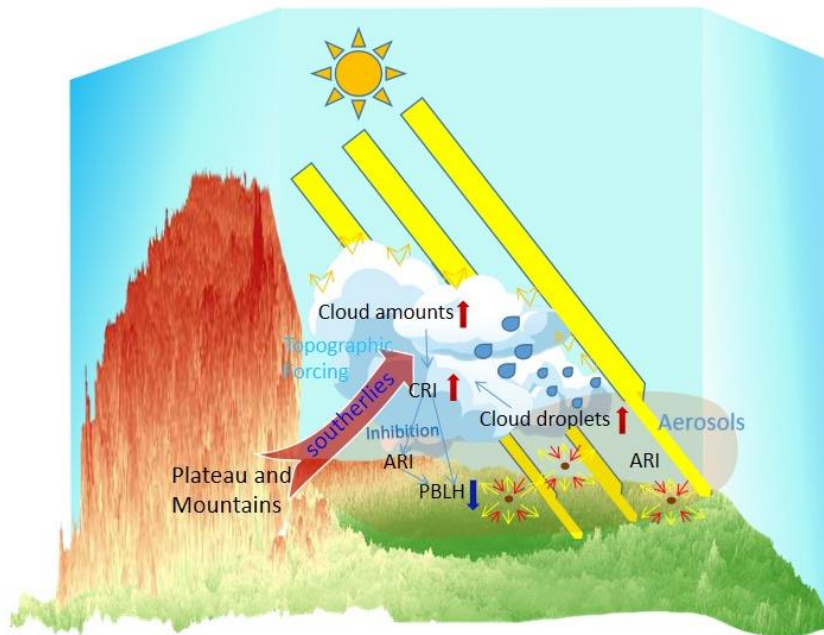
**Figure 12**. The aerosol radiative effect can be signigicantly inhibitted by cloud under influence of pollution synoptic patterns with dense cloud.

528

## 4 Conclusion

530   This study utilized synoptic classification and numerical simulation to gain insights in to the
531  combined effects of synoptic patterns and CRI inhibition on ARI and PBL structures in the wet and
532  cloudy SCB. Based on the long–term $PM_{2.5}$ observations and sounding data in the SCB, it was
533  found that large-scale synoptic circulations at 850 hPa played crucial roles in the variations of
534  $PM_{2.5}$ pollution. Synoptic classification was performed with the T-PCA method, which reveaed
535  that Pattern 2 and 5 characterized with low pressure system and southerly airflow on 850 hPa were
536  key synoptic patterns for onset and accumulation of $PM_{2.5}$, while Pattern 1 controlled by the
537  northerly airflow represented a clean pattern associated with significant decrease in $PM_{2.5}$.
538  Moreover, it was indicated that Pattern 2 and 5 exhibited denser cloud liquid water content and
539  thus stronger compared to other patterns. Among these patterns, Pattern 5 exhibited the highest
540  cloud liquid water content and CRI. This could be attributed to the robust southerly airflow
541  induced by the dense isobaric lines, which brought warm and humid air masses into the region.
542   To illustrate the interactions among cloud, aerosol and PBL under pollution synoptic patterns, a
543  pollution episode occurred from January 1 to 7, 2017, was simulated with using WRF-Chem. The

simulation results showed that ARI remarkably reduced solar radiation was during the two pollution patterns. This reduction led to surface cooling in the morning and upper–air warming in the afternoon. Additionally, the enhanced evening surface cooling was impacted by the mountain–valley wind circulations forced by the plateau–basin topography of the SCB. This modulation in the vertical thermal structure by the ARI would then suppress the development of the PBL, favoring pollution outbreaks (Fig. 12). Furthermore, parallel simulation experiments indicated that CRI impacted stratification stability and modulated the vertical thermal structure by inhibiting ARI (Fig. 12). Regarding the spatial distribution, a stronger ARI appeared in Chongqing, despite lower $PM_{2.5}$ concentrations compared to the western and southern SCB. This was due to the lower cloud liquid water content and weaker CRI inhibition of ARI in Chongqing. When CRI inhibition was not considered, the ARI in the western and southern SCB was significantly stronger than that in Chongqing. In addition, under Pattern 5, the reduction in solar radiation and PBLH during the daytime due to ARI could be more than doubled when the CRI influence was neglected. This was primarily due to higher aerosol concentrations and cloud liquid water contents associated with a low trough in Pattern 5. This study provided insights into the interaction among aerosols, clouds, and PBL under different synoptic patterns, considering the complex terrain and foggy/cloudy climate of the SCB. The findings highlighted the significant role of CRI inhibition on ARI during wet and cloudy conditions, shedding light in the multi-scale atmospheric physical processes in the SCB.

**Author contributions.** HL and MX had the original idea for the study, designed the experiments, conducted the numerical simulation and prepared the initial draft manuscript.  BL, YZ and KZ collected the data. TW and BZ helped perform the analysis with constructive discussions, reviewed and edited the manuscript. HL, MX, TW and BL acquired financial support for the project leading to this publication. SL and ML  reviewed the manuscript.

**Competing Interest:** The authors declare no conflict of interest.

**Data Available Statement**

The ERA5 pressure layer and single layer data  can be respectively downloaded from https://cds.climate.copernicus.eu/cdsapp#!/dataset/reanalysis-era5-pressure-levels                and https://cds.climate.copernicus.eu/cdsapp#!/dataset/reanalysis-era5-single-levels?tab=form. The NCEP FNL data are available at https://rda.ucar.edu/datasets/ds083.2/. The MEIC data can be accessed in Zheng et al (2018) at https://doi.org/10.5194/acp-18-14095-2018. Air quality and meteorological monitoring data can be acquired from https://doi.org/10.7910/DVN/USX59F.

**Financial support:** This work was supported by the National Natural Science Foundation of China (42205186), the Chongqing Natural Science Foundation (cstc2021jcyj-msxmX1007),   the open research fund of Chongqing Meteorological Bureau (KFJJ-201607) and the key technology research and development of Chongqing Meteorological Bureau (YWJSGG-202215; YWJSGG-202303).

580 **References**

581 Alexeeff, S., Deosaransingh, K., Liao, N., Van Den Eeden, S., Schwartz, J., and Sidney, S. (2021) Particulate
582    Matter and Cardiovascular Risk in Adults with Chronic Obstructive Pulmonary Disease, American
583    journal of respiratory and critical care medicine 204(2): 159-167.

584 Cao, S., Zhang, S., Gao, C., Yan, Y., Bao, J., Su, L., Liu, M., Peng, N., and Liu, M. (2021) A long-term analysis of
585    atmospheric black carbon MERRA-2 concentration over China during 1980–2019, Atmospheric
586    Environment 264, 118662.

587 Chen, Z., Chen, D., Zhao, C., Kwan, M.-p., Cai, J., Zhuang, Y., Zhao, B., Wang, X., Chen, B., Yang, J., Li, R., He,
588    B., Gao, B., Wang, K., and Xu, B. (2020) Influence of meteorological conditions on $PM_{2.5}$
589    concentrations across China: A review of methodology and mechanism, Environment International 139,
590    105558.

591 Ding, A., Huang, X., Nie, W., Sun, J., Kerminen, V.-M., Petäjä, T., Su, H., Cheng, Y., Yang, X.-Q., Wang, M.,
592    Chi, X., Wang, J. P., Virkkula, A., Guo, W., Yuan, J., Wang, S., Zhang, R. J., Wu, Y., Song, Y., and Fu,
593    C. (2016) Black carbon enhances haze pollution in megacities in China, Geophysical Research Letters
594    43(6):2873-2879.

595 ECMWF (2017). Part IV: Physical processes, In IFS documentation CY43R3 (pp. 1–221). England: European
596    Centre for Medium-Range Weather Forecasts. Retrieved from https://www.ecmwf.int/node/17736.

597 Eresmaa, N., Karppinen, A., Joffre, S. M., Räsänen, J., & Talvitie, H. (2006). Mixing height determination by
598    ceilometer. Atmos. Chem. Phys., 6(6), 1485-1493. https://doi.org/10.5194/acp-6-1485-2006.

599 Fast, J. D., Gustafson, W. I., Easter, R. C., Zaveri, R. A., Barnard, J. C., Chapman, E. G., Grell, G. A., and
600    Peckham, S. E.: Evolution of ozone, particulates, and aerosol direct radiative forcing in the vicinity of
601    Houston using a fully coupled meteorology-chemistry-aerosol model, J. Geophys. Res.-Atmos., 111,
602    D21305, https://doi.org/10.1029/2005jd006721, 2006.

603 Feng, X., Wei, S., and Wang, S. (2020) Temperature inversions in the atmospheric boundary layer and lower
604    troposphere over the Sichuan Basin, China: Climatology and impacts on air pollution, Science of The
605    Total Environment 726, 138579.

606 Garratt, J. R. (1994) Review: the atmospheric boundary layer, Earth-Science Reviews 37, 89-134.

607 Gong S, Liu Y, He J, Zhang L, Lu S, Zhang X. (2022)Multi-scale analysis of the impacts of meteorology and
608    emissions on $PM_{2.5}$ and $O_3$ trends at various regions in China from 2013 to 2020 1: Synoptic circulation
609    patterns and pollution. Sci Total Environ. Apr 1;815:152770.

610 Grell, G. A., Peckham, S. E., Schmitz, R., McKeen, S. A., Frost, G., Skamarock, W. C., and Eder, B. (2005) Fully
611    coupled "online" chemistry within the WRF model, Atmospheric Environment 39, 6957-6975.

612 Grell, G. A., & Freitas, S. R. (2013). A scale and aerosol aware convective parameterization. Atmos. Chem. Phys,
613    14(10), 5233–5250.

614 Guenther, A., Karl, T., Harley, P., Wiedinmyer, C., Palmer, P. I., and Geron, C. (2006) Estimates of global
615    terrestrial isoprene emissions using MEGAN (Model of Emissions of Gases and Aerosols from Nature),
616    Atmos. Chem. Phys. 6, 3181-3210.

617 Guo, J., Miao, Y., Zhang, Y., Liu, H., Li, Z., Zhang, W., ... & Zhai, P. (2016) The climatology of planetary
618    boundary layer height in China derived from radiosonde and reanalysis data. Atmospheric Chemistry and
619    Physics, 16(20), 13309-13319.

620 Hansen, J., Sato, M., and Ruedy, R. (1997) Radiative forcing and climate response, 102, 6831-6864.

621 Haywood, J. M., Abel, S. J., Barrett, P. A., Bellouin, N., Blyth, A., Bower, K. N., Brooks, M., Carslaw, K., Che,
622    H., Coe, H., Cotterell, M. I., Crawford, I., Cui, Z., Davies, N., Dingley, B., Field, P., Formenti, P.,
623    Gordon, H., de Graaf, M., Herbert, R., Johnson, B., Jones, A. C., Langridge, J. M., Malavelle, F.,
624    Partridge, D. G., Peers, F., Redemann, J., Stier, P., Szpek, K., Taylor, J. W., Watson-Parris, D., Wood, R.,

625    Wu, H., and Zuidema, P. (2021) The CLoud–Aerosol–Radiation Interaction and Forcing: Year 2017

626       (CLARIFY-2017) measurement campaign, Atmos. Chem. Phys. 21, 1049-1084.

627  Hong, S.-Y., Dudhia, J., and Chen, S.-H. (2004) A Revised Approach to Ice Microphysical Processes for the Bulk

628       Parameterization of Clouds and Precipitation, Monthly Weather Review 132, 103-120.

629  Hong, S. Y., Y. Noh, and J. Dudhia (2006), A new vertical diffusion package with an explicit treatment of

630       entrainment processes, Mon. Weather Rev., 134(9), 2318-2341.

631  Hu, J., Zhao, T., Liu, J., Cao, L., Xia, J., Wang, C., Zhao, X., Gao, Z., Shu, Z., and Li, Y. (2021) Nocturnal surface

632       radiation cooling modulated by cloud cover change reinforces $PM_{2.5}$ accumulation: Observational study

633       of heavy air pollution in the Sichuan Basin, Southwest China, Science of The Total Environment 794,

634       148624.

635  Huth, R. (1996) AN INTERCOMPARISON OF COMPUTER-ASSISTED CIRCULATION CLASSIFICATION

636       METHODS, International Journal of Climatology 16, 893-922.

637  Huth, R., Beck, C., Philipp, A., Demuzere, M., Ustrnul, Z., Cahynová, M., Kyselý, J., and Tveito, O. E. (2008)

638       Classifications of Atmospheric Circulation Patterns, Ann N Y Acad Sci, 1146, 105-152.

639  Iacono, M. J., Delamere, J. S., Mlawer, E. J., Shephard, M. W., Clough, S. A., and Collins, W. D. (2008),

640       Radiative forcing by long-lived greenhouse gases: Calculations with the AER radiative transfer models, J.

641       Geophys. Res., 113, D13103.

642  Jiang, Y., Xin, J., Zhao, D., Jia, D., Tang, G., Quan, J., Wang, M., & Dai, L. (2021). Analysis of differences

643       between thermodynamic and material boundary layer structure: Comparison of detection by ceilometer

644       and microwave radiometer. Atmospheric Research, 248, 105179.

645       ttps://doi.org/https://doi.org/10.1016/j.atmosres.2020.105179.

646  Jiménez, P. A., & Dudhia, J. (2012). Improving the Representation of Resolved and Unresolved Topographic

647       Effects on Surface Wind in the WRF Model. Journal of Applied Meteorology and Climatology, 51(2),

648       300-316. https://doi.org/https://doi.org/10.1175/JAMC-D-11-084.1.

649  Li, K., Liao, H., Mao, Y., and Ridley, D. A. (2016) Source sector and region contributions to concentration and

650       direct radiative forcing of black carbon in China, Atmospheric Environment 124, 351-366.

651  Li, J., Wu, M., Li, Y., Ma, S., Wang, Z., Zhao, Y., et al. (2021a). Reinforcement of secondary circulation by

652       aerosol feedback and $PM_{2.5}$ vertical exchange in the atmospheric boundary layer. Geophysical Research

653       Letters, 48, e2021GL094465.

654  Li, Q., Wu, B., Liu, J., Zhang, H., Cai, X., and Song, Y. (2020) Characteristics of the atmospheric boundary layer

655       and its relation with $PM_{2.5}$ during haze episodes in winter in the North China Plain, Atmospheric

656       Environment 223, 117265.

657  Li, X., Miao, Y., Ma, Y., Wang, Y., and Zhang, Y. (2021b) Impacts of synoptic forcing and topography on aerosol

658       pollution during winter in Shenyang, Northeast China, Atmospheric Research 262, 105764.

659  Li, Z., Wang, Y., Guo, J., Cribb, M., Dong, X., Fan, J., Gong, D.-Y., Huang, J., Jiang, M., Jiang, Y., Lee, S. S., Li,

660       H., Li, J., Liu, J., Qian, Y., Rosenfeld, D., Shan, S., Sun, Y., Wang, H., and Zheng, Y. (2019) East Asian

661       Study of Tropospheric Aerosols and their Impact on Regional Clouds, Precipitation, and Climate

662       (EAST-AIR CPC ), Journal of Geophysical Research: Atmospheres 124(23):13026-13054.

663  Liao, Z., Jielan, X., Fang, X., Wang, Y., Zhang, Y., Xu, X., and Fan, S. (2020) Modulation of synoptic circulation

664       to dry season $PM_{2.5}$ pollution over the Pearl River Delta region: An investigation based on self-

665       organizing maps, Atmospheric Environment 230, 117482.

666  Liu, N., Zhou, S., Liu, C., and Guo, J. (2019) Synoptic circulation pattern and boundary layer structure associated

667       with $PM_{2.5}$ during wintertime haze pollution episodes in Shanghai, Atmospheric Research 228, 186-195.

668  Lohmann, U., and Feichter, J. (2005) Global indirect aerosol effects: a review, Atmos. Chem. Phys. 5, 715-737.

669 Lu H, Xie M, Liu B, Liu X, Feng J, Yang F, Zhao X, You T, Wu Z, Gao Y. (2022) Impact of atmospheric
670   thermodynamic structures and aerosol radiation feedback on winter regional persistent heavy particulate
671   pollution in the Sichuan-Chongqing region, China. Sci Total Environ.  Oct 10;842:156575.

672 Lu, H., Xie, M., Liu, X., Liu, B., Jiang, M., Gao, Y., & Zhao, X. (2021). Adjusting prediction of ozone
673   concentration based on CMAQ model and machine learning methods in Sichuan-Chongqing region,
674   China. Atmospheric Pollution Research, 12(6), 101066.
675   https://doi.org/https://doi.org/10.1016/j.apr.2021.101066.

676 Ma, S., Shao, M., Zhang, Y., Dai, Q., and Xie, M. (2021) Sensitivity of $PM_{2.5}$ and $O_3$ pollution episodes to
677   meteorological factors over the North China Plain, Science of The Total Environment 792, 148474.

678 Miao, Y., Che, H., Zhang, X., and Liu, S. (2020) Integrated impacts of synoptic forcing and aerosol radiative effect
679   on boundary layer and pollution in the Beijing–Tianjin–Hebei region, China, Atmos. Chem. Phys. 20,
680   5899-5909.

681 Miao, Y., Che, H., Zhang, X., and Liu, S. (2021) Relationship between summertime concurring $PM_{2.5}$ and $O_3$
682   pollution and boundary layer height differs between Beijing and Shanghai, China, Environmental
683   Pollution 268, 115775.

684 Miao, Y., Guo, J., Liu, S., Liu, H., Li, Z., Zhang, W., and Zhai, P. (2017) Classification of summertime synoptic
685   patterns in Beijing and their associations with boundary layer structure affecting aerosol pollution,
686   Atmospheric Chemistry and Physics 17, 3097-3110.

687 Nandan, R., Madineni, V. R., Kiran, R., & Naik, D. (2021). Retrieval of cloud liquid water path using radiosonde
688   measurements: Comparison with MODIS and ERA5. Journal of Atmospheric and Solar-Terrestrial
689   Physics, 227, 105799. https://doi.org/10.1016/j.jastp.2021.105799.

690 Ning, G., Wang, S., Ma, M., Ni, C., Shang, Z., Wang, J., and Li, J. (2017) Characteristics of air pollution in
691   different zones of Sichuan Basin, China, The Science of the total environment 612, 975-984.

692 Ning, G., Yim, S. H. L., Wang, S., Duan, B., Nie, C., Yang, X., Wang, J., and Shang, K. (2019) Synergistic effects
693   of synoptic weather patterns and topography on air quality: a case of the Sichuan Basin of China,
694   Climate Dynamics 53, 6729-6744.

695 Ojo, J. S., Ayeni, D., & Ogunjo, S. T. (2023). Comparative analysis between ERA5 reanalysis data and MRR
696   observation data at different altitudes for fall velocity and liquid water content. Advances in Space
697   Research, 72(6), 2217-2225. https://doi.org/https://doi.org/10.1016/j.asr.2023.05.045.

698 Painemal, D., Chellappan, S., Smith, W. L. Jr., Spangenberg, D., Park, J. M., Ackerman, A., et al. (2023).
699   Wintertime synoptic patterns of midlatitude boundary layer clouds over the western North Atlantic:
700   Climatology and insights from in situ ACTIVATE observations. Journal of Geophysical Research:
701   Atmospheres, 128, e2022JD037725. https://doi. org/10.1029/2022JD037725.

702 Peng, J., Hu, M., Shang, D., Wu, Z., Du, Z., Tan, T., Wang, Y., Zhang, F., & Zhang, R. (2021). Explosive
703   Secondary Aerosol Formation during Severe Haze in the North China Plain. Environmental Science &
704   Technology, 55(4), 2189-2207. https://doi.org/10.1021/acs.est.0c07204.

705 Pilinis, C., Seinfeld, J. H., and Grosjean, D. (1989) Water content of atmospheric aerosols, Atmospheric
706   Environment 23, 1601-1606.

707 Pöschl, U., Martin, S. T., Sinha, B., Chen, Q., Gunthe, S. S., Huffman, J. A., Borrmann, S., Farmer, D. K., Garland,
708   R. M., Helas, G., Jimenez, J. L., King, S. M., Manzi, A., Mikhailov, E., Pauliquevis, T., Petters, M. D.,
709   Prenni, A. J., Roldin, P., Rose, D., Schneider, J., Su, H., Zorn, S. R., Artaxo, P., and Andreae, M. O.
710   (2010) Rainforest Aerosols as Biogenic Nuclei of Clouds and Precipitation in the Amazon, 329, 1513-
711   1516.

712 Qi, N.; Tan, X.; Wu, T.; Tang, Q.; Ning, F.; Jiang, D.; Xu, T.; Wu, H.; Ren, L. (2022) Deng, W. Temporal and
713   Spatial Distribution Analysis of Atmospheric Pollutants in Chengdu–Chongqing Twin-City Economic
714   Circle. Int. J. Environ. Res. Public Health, 19, 4333. https://doi.org/10.3390/ijerph19074333.

715 Rosenfeld, D., Lohmann, U., Raga, G. B., O'Dowd, C. D., Kulmala, M., Fuzzi, S., Reissell, A., and Andreae, M. O.
716   (2008) Flood or Drought: How Do Aerosols Affect Precipitation?, Science 321, 1309-1313.

717 Seibert, P., Beyrich, F., Gryning, S.-E., Joffre, S., Rasmussen, A., & Tercier, P. (2000). Review and
718   intercomparison of operational methods for the determination of the mixing height. Atmospheric
719   Environment, 34(7), 1001-1027. https://doi.org/https://doi.org/10.1016/S1352-2310(99)00349-0.

720 Schell, B., Ackermann, I. J., Hass, H., Binkowski, F. S., and Ebel, A. (2001) Modeling the formation of secondary
721   organic aerosol within a comprehensive air quality model system, Journal of Geophysical Research:
722   Atmospheres 106, 28275-28293.

723 Scott Archer-Nicholls, Douglas Lowe, David M. Schultz, and Gordon McFiggans. (2016)Aerosol–radiation–cloud
724   interactions in a regional coupled model: the effects of convective parameterisation and resolution,
725   Atmos. Chem. Phys., 16, 5573–5594.

726 Shu, Z., Liu, Y., Zhao, T., Xia, J., Wang, C., Cao, L., Wang, H., Zhang, L., Zheng, Y., Shen, L., Luo, L., and Li, Y.
727   (2021) Elevated 3D structures of $PM_{2.5}$ and impact of complex terrain-forcing circulations on heavy haze
728   pollution over Sichuan Basin, China, Atmos. Chem. Phys. 21, 9253-9268.

729 Skamarock, W. C., Klemp, J. B., Dudhia, J., Gill, D. O., Barker, D., Duda, M. G., … Powers, J. G. (2008). A
730   Description of the Advanced Research WRF Version 3 (No. NCAR/TN-475+STR). University
731   Corporation for Atmospheric Research. doi:10.5065/D68S4MVH.

732 Stockwell, W. R., Middleton, P., Chang, J. S., and Tang, X. (1990) The second generation regional acid deposition
733   model chemical mechanism for regional air quality modeling, Journal of Geophysical Research:
734   Atmospheres 95, 16343-16367.

735 Su, T., Li, Z., and Kahn, R. (2018) Relationships between the planetary boundary layer height and surface
736   pollutants derived from lidar observations over China: regional pattern and influencing factors, Atmos.
737   Chem. Phys. 18, 15921-15935.

738 Tewari, M., Chen, F., Wang, W., Dudhia, J., Lemone, M. A., … Mitchell, K. E. (2004). Implementation and
739   verification of the unified Noah land-surface model in the WRF model [presentation]. In 20th
740   Conference on Weather Analysis and Forecasting/16th Conference on Numerical Weather Prediction.
741   American Meteorological Society: Seattle, WA, US.

742 Twomey, S. (1977) The Influence of Pollution on the Shortwave Albedo of Clouds, Journal of Atmospheric
743   Sciences 34, 1149-1152.

744 Wang, C., Jia, M., Xia, H., Wu, Y., Wei, T., Shang, X., Yang, C., Xue, X., and Dou, X. (2019) Relationship
745   analysis of $PM_{2.5}$ and boundary layer height using an aerosol and turbulence detection lidar, Atmos.
746   Meas. Tech. 12, 3303-3315.

747 Wang, D., Jensen, M. P., Taylor, D., Kowalski, G., Hogan, M., Wittemann, B. M., Rakotoarivony, A., Giangrande,
748   S. E., and Park, J. M. (2022) Linking Synoptic Patterns to Cloud Properties and Local Circulations Over
749   Southeastern Texas, Journal of Geophysical Research: Atmospheres 127, e2021JD035920.

750 Wang, P., Qiao, X., & Zhang, H. (2020). Modeling $PM_{2.5}$ and $O_3$ with aerosol feedbacks using WRF/Chem over
751   the Sichuan Basin, southwestern China. Chemosphere, 254, 126735.
752   https://doi.org/https://doi.org/10.1016/j.chemosphere.2020.126735.

753 Wang, Z., Huang, X., and Ding, A. (2018) Dome effect of black carbon and its key influencing factors: a one-
754   dimensional modelling study, Atmos. Chem. Phys. 18, 2821-2834.

755 Wang, Y., Gao, W., Wang, S., Song, T., Gong, Z., Ji, D., Wang, L., Liu, Z., Tang, G., Huo, Y., Tian, S., Li, J., Li,
756   M., Yang, Y., Chu, B., Petäjä, T., Kerminen, V.-M., He, H., Hao, J., Kulmala, M., Wang, Y., and Zhang,

757        Y. (2020) Contrasting trends of $PM_{2.5}$ and surface-ozone concentrations in China from 2013 to 2017,
758        National Science Review 7, 1331-1339.

759 Wu, Z., Xie, M., Gao, Y., Lu, H., Zhao, L., Gao, S., (2018). Inversion of $SO_2$ emissions over chongqing with
760        ensemble square root kalman filter. Research of Environmental Sciences 31, 25–33.

761 Xiao, Q., Zheng, Y., Geng, G., Chen, C., Huang, X., Che, H., Zhang, X., He, K., and Zhang, Q. (2021) Separating
762        emission and meteorological contributions to long-term $PM_{2.5}$ trends over eastern China during 2000–
763        2018, Atmos. Chem. Phys. 21, 9475-9496.

764 Xie, M., Liao, J., Wang, T., Zhu, K., Zhuang, B., Han, Y., Li, M., and Li, S. (2016) Modeling of the anthropogenic
765        heat flux and its effect on regional meteorology and air quality over the Yangtze River Delta region,
766        China, Atmospheric Chemistry and Physics 16, 6071-6089.

767 Xie, M., Zhu, K., Wang, T., Feng, W., Gao, D., Li, M., Li, S., Zhuang, B., Han, Y., Chen, P., and Liao, J. (2016)
768        Changes in regional meteorology induced by anthropogenic heat and their impacts on air quality in
769        South China, Atmos. Chem. Phys. 16, 15011-15031.

770 Xu, Y., Xue, W., Lei, Y., Huang, Q., Zhao, Y., Cheng, S., Ren, Z., and Wang, J. (2020) Spatiotemporal variation
771        in the impact of meteorological conditions on $PM_{2.5}$ pollution in China from 2000 to 2017, Atmospheric
772        Environment 223, 117215.

773 Yang, T., Chen, R., Gu, X., Xu, J., Yang, L., Zhao, J., Zhang, X., Bai, C., Kang, J., Ran, P., Shen, H., Wen, F.,
774        Huang, K., Chen, Y., Sun, T., Shan, G., Lin, Y., Wu, S., Zhu, J., Wang, R., Shi, Z., Xu, Y., Ye, X., Song,
775        Y., Wang, Q., Zhou, Y., Ding, L., Yang, T., Yao, W., Guo, Y., Xiao, F., Lu, Y., Peng, X., Zhang, B.,
776        Xiao, D., Wang, Z., Zhang, H., Bu, X., Zhang, X., An, L., Zhang, S., Cao, Z., Zhan, Q., Yang, Y., Liang,
777        L., Cao, B., Dai, H., van Donkelaar, A., Martin, R. V., Wu, T., He, J., Kan, H., and Wang, C. (2021)
778        Association of fine particulate matter air pollution and its constituents with lung function: The China
779        Pulmonary Health study, Environment International 156, 106707.

780 Yang Dasheng, Wang Pucai. 2012. Characteristics of Vertical Distributions of Cloud Water Contents over China
781        during Summer. Chinese Journal of Atmospheric Sciences, 36(1): 89-101.

782 Yao, B., Liu, C., Yin, Y., Liu, Z., Shi, C., Iwabuchi, H., & Weng, F. (2020). Evaluation of cloud properties from
783        reanalyses over East Asia with a radiance-based approach. Atmos. Meas. Tech., 13(3), 1033-1049.
784        https://doi.org/10.5194/amt-13-1033-2020.

785 Yin, Z., and Wang, H. (2017) Role of atmospheric circulations in haze pollution in December 2016, Atmos. Chem.
786        Phys. 17, 11673-11681.

787 Yu, R., Wang, B., and Zhou, T. (2004) Climate Effects of the Deep Continental Stratus Clouds Generated by the
788        Tibetan Plateau, Journal of Climate 17, 2702-2713.

789 Zhan, C.-c., Xie, M., Fang, D.-x., Wang, T., Wu, Z., Lu, H., Li, M.-m., Chen, P., Zhuang, B.-l., Li, S., Zhang, Z.-q.,
790        Gao, D., Reng, J.-y., and Zhao, M. (2019) Synoptic weather patterns and their impacts on regional
791        particle pollution in the city cluster of the Sichuan Basin, China, Atmospheric Environment 208(1): 34-
792        47.

793 Zhan, C., Xie, M., Lu, H., Liu, B., Wu, Z., Wang, T., Zhuang, B., Li, M., and Li, S.(2023) Impacts of urbanization
794        on air quality and the related health risks in a city with complex terrain, Atmos. Chem. Phys., 23, 771–
795        788,

796 Zhang, J., Lin, Z., 1985. Climate in China. Shanghai Publication House, Shanghai, p. 603.

797 Zhang, S., Zeng, G., Wang, T., Yang, X., and Iyakaremye, V. (2022) Three dominant synoptic atmospheric
798        circulation patterns influencing severe winter haze in eastern China, Atmos. Chem. Phys. 22, 16017-
799        16030.

800  Zhang, Y., Ding, A., Mao, H., Nie, W., Zhou, D., Liu, L., Huang, X., and Fu, C. (2015) Impact of synoptic weather
801      patterns and inter-decadal climate variability on air quality in the North China Plain during 1980–2013,
802      Atmospheric Environment 124, Part B: 119-128.

803  Zhao, B., Liou, K.-N., Gu, Y., Li, Q., Jiang, J. H., Su, H., He, C., Tseng, H.-L. R., Wang, S., Liu, R., Qi, L., Lee,
804      W.-L., and Hao, J. (2017) Enhanced $PM_{2.5}$ pollution in China due to aerosol-cloud interactions,
805      Scientific Reports 7, 4453.

806  Zhao, C., Yang, Y., Fan, H., Huang, J., Fu, Y., Zhang, X., Kang, S., Cong, Z., Letu, H., and Menenti, M. (2020)
807      Aerosol characteristics and impacts on weather and climate over the Tibetan Plateau, National Science
808      Review 7, 492-495.

809  Zhao, S., Yu, Y., Yin, D., Qin, D., He, J., and Dong, L. (2017) Spatial patterns and temporal variations of six
810      criteria air pollutants during 2015 to 2017 in the city clusters of Sichuan Basin, China, The Science of
811      the total environment 624, 540-557.

812  Zheng, B., Tong, D., Li, M., et al. (2018) Trends in China's anthropogenic emissions since 2010 as the
813      consequence of clean air actions, Atmos. Chem. Phys., 18, 14095-14111.

814  Zhong, J., Zhang, X., Wang, Y., Wang, J., Shen, X., Zhang, H., Wang, T., Xie, Z., Liu, C., Zhang, H., Zhao, T.,
815      Sun, J., Fan, S., Gao, Z., Li, Y., and Wang, L. (2019) The two-way feedback mechanism between
816      unfavorable meteorological conditions and cumulative aerosol pollution in various haze regions of China,
817      Atmospheric Chemistry and Physics 19, 3287-3306.

818  Zhong, J., Zhang, X., Yunsheng, D., Wang, Y., Liu, C., Wang, J., Zhang, Y., and Che, H. (2018) Feedback effects
819      of boundary-layer meteorological factors on cumulative explosive growth of $PM_{2.5}$ during winter heavy
820      pollution episodes in Beijing from 2013 to 2016, Atmospheric Chemistry and Physics 18, 247-258.

821  Zhou, M., Zhang, L., Chen, D., Gu, Y., Fu, T.-M., Gao, M., Zhao, Y., Lu, X., and Zhao, B. (2019) The impact of
822      aerosol–radiation interactions on the effectiveness of emission control measures, Environmental
823      Research Letters 14, 024002.